Pion-pion correlations at low relative momentum produced in p-p collisions at 27.5 GeV/c

J. Uribe,* E. P. Hartouni, D. A. Jensen,[†] and M. N. Kreisler
Department of Physics and Astronomy, University of Massachusetts, Amherst, Massachusetts 01003

M. D. Church,[†] E. E. Gottschalk,[‡] B. C. Knapp, W. Sippach, B. J. Stern,[§] and L. R. Wiencke[‖]
Columbia University, Nevis Laboratories, Irvington, New York 10533

D. C. Christian, G. Gutierrez, S. D. Holmes, and A. Wehmann
Fermilab, Batavia, Illinois 60510

C. Avilez[¶]
Instituto de Fisica, Universidad de Guanajuato, Leon, Gto., Mexico

M. Forbush,** F. R. Huson, and J. T. White
Department of Physics, Texas A&M University, College Station, Texas 77843

We have measured the momentum correlation of pion pairs produced in the collisions of 27.5 GeV/c protons in liquid hydrogen. By considering events for which all final state particles have been measured, we have succeeded in reducing backgrounds due to particle misidentification below 5% for π^+ and 1% for π^-. Our use of a precision magnetic spectrometer has provided an accurate determination of particle momenta and excellent acceptance for particle pairs with small relative momentum essential for correlations studies. A large data sample of fully reconstructed events (1×10^6) allows us to analyze the correlations for $\pi^+\pi^+$ and $\pi^-\pi^-$ pairs separately, and also as a function of the final state multiplicity. We find that the pion pair correlations scale 0.98 fm describes the data well. We do not find any indication of multiplicity dependence of the correlation scale for multiplicities from 6 to 14 final state particles.

PACS number(s): 13.85.Hd

I. INTRODUCTION

The observation of relative momentum correlations between pairs of like-sign pions in low-energy proton-antiproton reactions [1] was made in the late 1950s. A possible explanation of these correlations was proposed almost immediately in a paper by Goldhaber, Goldhaber, Lee, and Pais [2] (GGLP). In that paper the agreement between the data and a properly symmetrized statistical model [3] calculation provided compelling evidence that the correlations were due to the bosonic nature of pions. GGLP showed that identical particles emitted by separated sources will have correlated momenta. The exact form of the two-particle relative momentum probabil-

ity distribution depends on the detailed nature of the sources and their space-time configuration. GGLP assumed a simple Gaussian source distribution in the relative space-time position of the sources to ease calculational difficulties. This source distribution was then integrated over the "reaction volume" to provide a probability function which modified the pion kinematic variables. An assumption of the statistical model is that the square of the matrix element is independent of the kinematic variables of the initial state and final state particles. There is only one adjustable parameter in GGLP's analysis, the "radius" of the reaction volume.

Many other experiments observed pion correlations in low-energy interactions during the 1960s [4]. The comparison of these experimental results with theory is less compelling than the GGLP analysis due to the increasing complexity of the reactions, the existence of resonances, the existence of final state interactions, the increasing number of pions, and the inability to calculate the correlations.

The possibility of using the pion correlations to measure the space-time development of the hadronic interaction was proposed by Kopylov and Podgoretskii [5] (KP). This paper explored the effects of different source distributions on the correlations. More importantly, the idea of a "correlation function" containing information about the space-time development of the source was introduced. It was conjectured that the correlation function could be extracted from the measurements by examining the ratio

<u>49</u>   4373

of the data plotted in the correlation variable (e.g., the relative momenta) to a distribution in the same variable of events produced identically to the data *except for the correlations.*

Experiments [6] since KP have attempted to build the noncorrelated data sample either from the data (e.g., pairing pions from separate events, etc.) or from a Monte Carlo simulation of the data or from both. The ratio of correlated to uncorrelated distributions is then fit to a standard parametrization associated with the physical aspects of the pion sources. An enhanced probability of low-relative-momenta pairs is usually interpreted as the observation of the effect. Experiments analyzed in this manner using a variety of beam and target hadrons agree on the typical scale of the reaction volume radius, 1 fm.

Observing a change in the correlation may signal a change in the underlying dynamics of pion production. In particular, a change of state due to high-energy density reactions of nuclei [7] might be observed as a change in the pion relative-momenta correlation scale. It is the dependence of the correlation scale on nuclear atomic number [8] which provides the best evidence that pion correlations are actually measuring the source size. Of course, the behavior of the correlations depends on the details of the phase transitions. These details remain beyond the realm of our calculational ability.

There are several difficulties in observing correlations. The correlations in a sample can be "diluted" by the inclusion of misidentified particles. The existence of resonances which decay to pions can introduce kinematic correlations. Increasing the number of final state parti-

cles also increases the probability of final state interactions, which will affect the correlation distributions. Finally, it is difficult to find uncorrelated samples with which to compare the correlated sample. This last difficulty affects the parametrization used to describe the correlation and its physical interpretation.

This study attempts to resolve many of those difficulties. We use a very large data set of approximately 300×10^6 events produced in proton-proton interactions. These data come from the BNL E766 experiment, which employed a multiparticle spectrometer capable of precise momentum measurements of high-multiplicity (as many as 20 charged particles) reactions and efficient charged particle identification at high interaction rates (as high as 1 MHz).

The subset of data used in this study consists of events with two protons and charged pions for which all final state particles are measured. Here 10^6 events satisfied these selection criteria. The size of this data sample allows us to separate the sample into final state multiplicities and into charges of pion pairs. The ability to measure different final states within the same data sample reduces systematic uncertainties.

Doing the analysis as a function of the charge of the pion pair provides a check on the effect of backgrounds due to particle misidentification. The characteristics of the sources of the charged pions should be independent of the pion charge, a consequence of the charge invariance of the strong interaction. Thus the distributions for positively charged pairs should be identical to those of negatively charged pairs. In this experiment a major back-
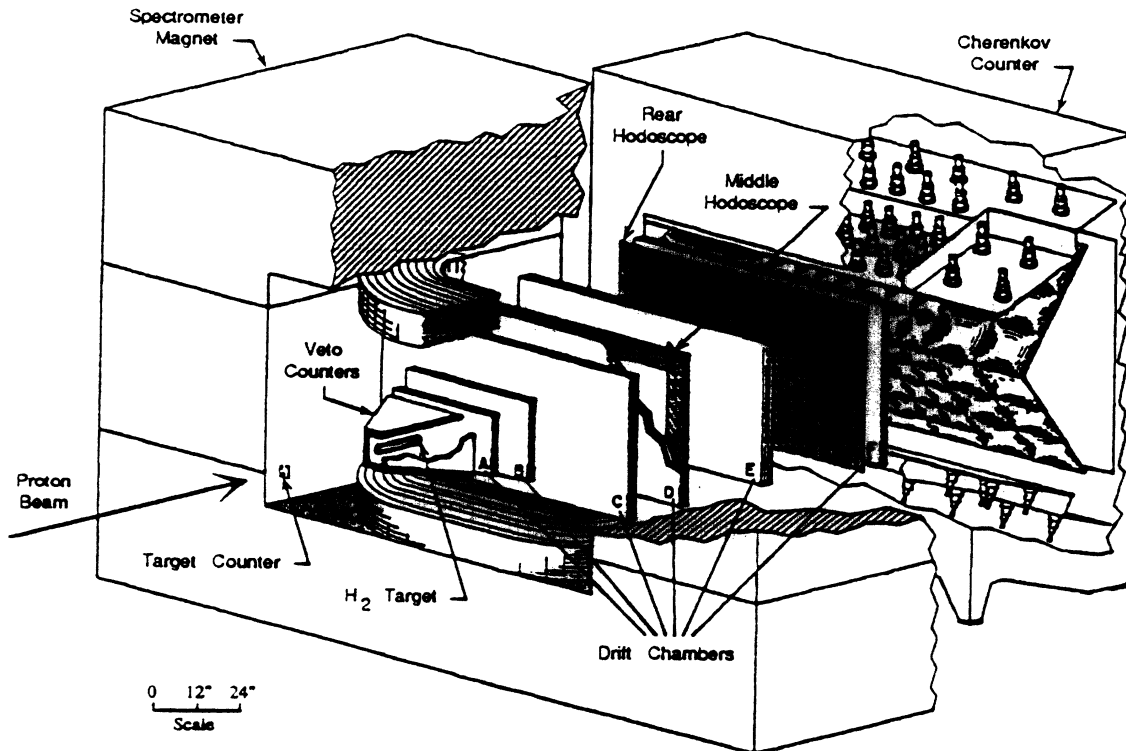

FIG. 1. A perspective view of the BNL E766 spectrometer. The drift chamber stations are labeled A–F.
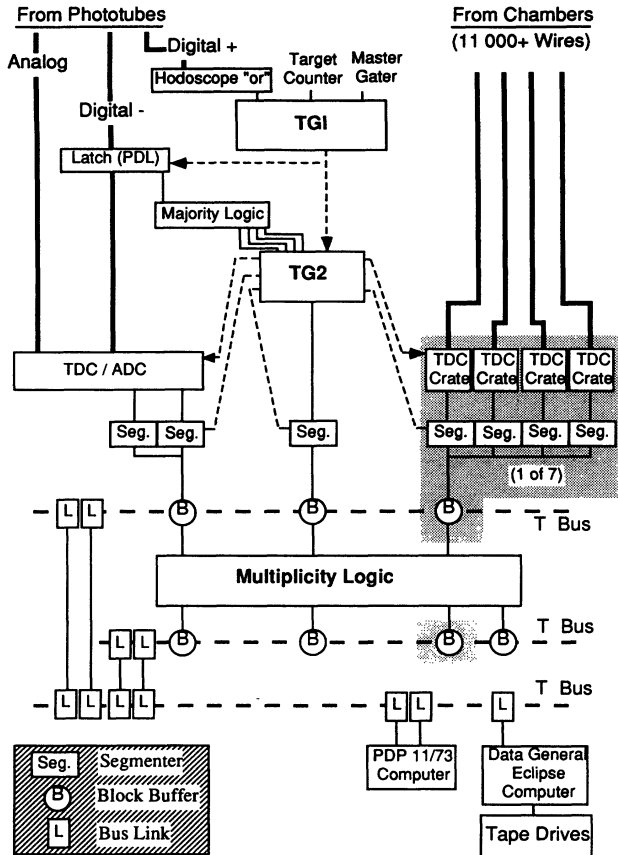
FIG. 2. Block diagram of BNL E766 data acquisition system.

ground to positively charged pions is misidentified protons. Particle identification is provided primarily by requiring the conservation of momentum and energy. Additional direct particle identification measurements reduce these backgrounds. Since negative pions cannot be mistaken for protons, the negative pion distributions provide checks on the positive pion distributions.

The pion pair correlations can be altered by the presence of resonances decaying to final states with charged pions. The measurement of all final state particles allows us to study the effects of resonance production on these correlations. Since all resonances produced in the in-

teractions are observed (though not on an event-by-event basis), the effect of the resonance decay kinematics on the pion distributions can be studied directly from these data.

The effects of final state interactions on the correlations can be studied with the data. The precision of the momentum measurement allows for the observation of correlations between pions due to electromagnetic final state interactions [9]. The sensitivity of the apparatus to these small effects gives an indication of our sensitivity to final state interactions.

It is necessary to compare the correlation distributions to that expected for an uncorrelated sample. This study of data consisting of fully reconstructed events rules out a "traditional" procedure for constructing the uncorrelated data sample. Because energy-momentum conservation has been required for each event, replacing a pion in one event with a pion chosen randomly from another event would violate momentum-energy conservation for the event. We have chosen instead to compare the correlation distributions to "uncorrelated" distributions produced by Lorentz-invariant phase space (LIPS). This choice has two major advantages: (1) The procedure is simple to explain and interpret and (2) the result is model independent. This second point is particularly compelling given the lack of either a calculable fundamental theory of interactions at these energies or of a believable empirical model. The statement of our results in terms of LIPS should allow a comparison with future calculations.

The use of fully reconstructed events presents some new complications in the analysis of pion correlations. However, using fully reconstructed events decreases particle identity backgrounds by *an order of magnitude* over studies using inclusive pion pairs. It is our opinion that this benefit outweighs the problems of a more complex analysis.

II. APPARATUS

The BNL E766 apparatus was designed as a general purpose multiparticle spectrometer. The ability to reconstruct all of the charged particles from nucleon-proton interactions efficiently and precisely was a central design goal. To obtain large numbers of events to perform high-sensitivity searches and precise, background-free, measurements required an apparatus capable of operating

TABLE I. Total numbers of events of the reaction types (1a)–(1e) as a function of the final selection criteria.

	Multiplicity $(2+2m)$					
	6	8	10	12	14	Total
One vertex events	209 512	1 051 449	581 092	129 761	16 680	1 988 494
Events after cut of $(\sum \mathbf{p}_\perp)^2$ ≤ 0.0016 $(GeV/c)^2$	129 615	717 663	394 255	87 277	10 264	1 339 074
Events with at least one $pp\ m\pi^+ m\pi^-$ solution and $-8 \leq \Delta(E-P_z) \leq +13$ MeV	81 549	542 263	319 818	74 171	8973	1 026 774
Events after direct particle identification	73 770	469 363	267 307	61 608	7689	879 737
Number of $pp\ m\pi^+ m\pi^-$ solutions/event	1.07	1.19	1.24	1.29	1.36	

at high interaction rates for prolonged running periods.

The apparatus was located in the B-5 external beam line of the Brookhaven National Laboratory (BNL) Alternating Gradient Synchrotron (AGS). This beam line was configured to provide a high-flux (10^{12}/s) proton beam with a nominal momentum of 28 GeV/c. The beam-line design minimized beam halo. The intensity of this beam was controlled by passing the beam through a wedge-shaped copper "degrader." The beam emerged from this degrader with a momentum of 27.5 GeV/c. The proton flux at the BNL E766 target was 10^7/s. The beam had a 1-in. square profile at the target.

The momenta of the beam particles were determined by a set of four drift chambers and a string of dipole magnets. These were located between the degrader and the experiment's target. This beam spectrometer determined the slope of the incident proton beam to $\pm 10^{-4}$ rad horizontally and $\pm 10^{-3}$ rad vertically. The momentum resolution of the beam spectrometer was ± 300 MeV/c. The target region consisted of a "thin" (5% interaction length) liquid hydrogen target and a system of scintillation counters. These counters were used to detect the presence of a beam proton (and define the event's "initial" time) and to provide signals making it possible to veto particles passing outside of the apparatus' geometric acceptance. Figure 1 depicts the target counter, target, and veto box in relationship to the rest of the apparatus.

The multiparticle spectrometer consisted of five stations of drift chambers contained within the aperture of a large magnet (called the "Jolly Green Giant") and one drift chamber station located downstream of the
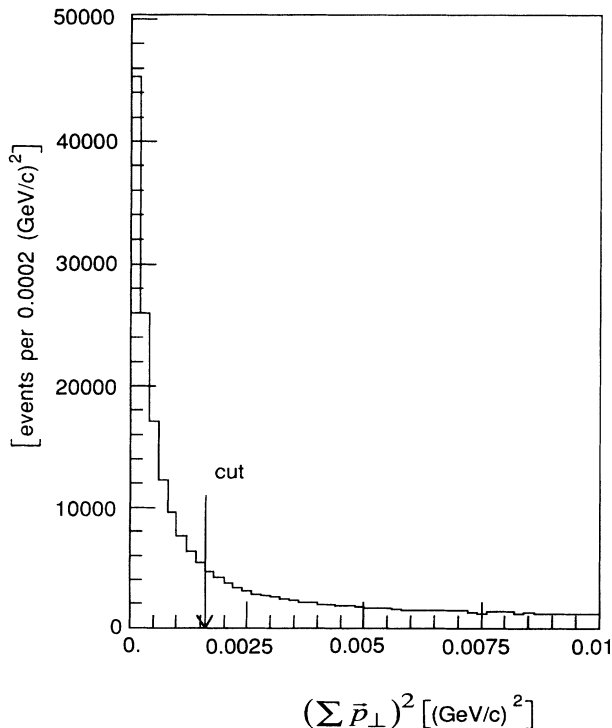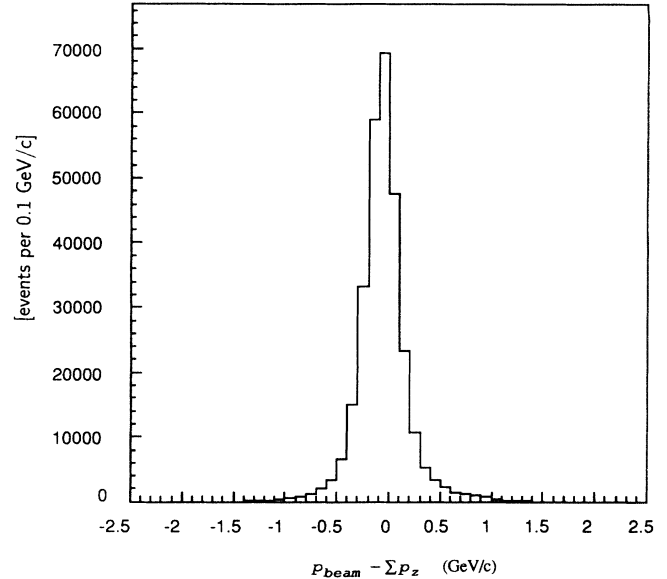

FIG. 4. Distribution of the difference between the beam momentum and the sum of the final state longitudinal momentum. Fully reconstructed events are defined to lie between the cuts indicated by arrows.

magnet's aperture. Each drift chamber consisted of four planes oriented at $\pm 7°$ and $\pm 21°$ to the vertically oriented magnetic field. The drift chamber electrostatic structure was that of a proportional wire chamber (PWC): alternating planes of cathodes and anodes. The anode-to-anode wire spacing varied from 2 mm in the chamber closest to the target to 3.5 mm in the furthest chamber.

FIG. 3. $(\sum \mathbf{p}_{\perp i})^2$ distribution of six-track single-vertex events which are candidates for the topology of reaction (1a).
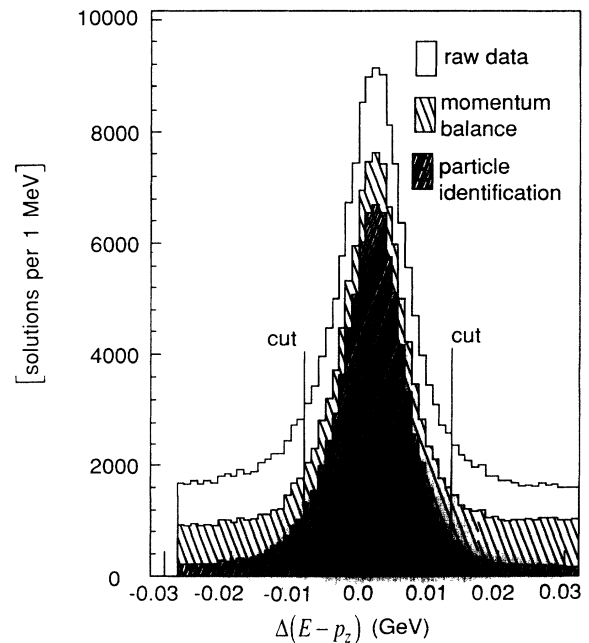

FIG. 5. $\Delta(E - p_z)$ distributions for events which are candidates for reaction (1a). The effect of cuts imposing transverse momentum conservation and agreement with direct particle identification are indicated. Arrows indicate final sample cuts.

TABLE II. Estimates of backgrounds for reactions (1a)–(1e) designated by multiplicity.

	Multiplicity $(2+2m)$				
	6	8	10	12	14
Selected events	73 710	469 363	267 307	61 608	7689
Number of pp $m\pi^+ m\pi^-$ solutions	75 789	495 097	291 520	69 398	8810
$\Delta(E-P_z)$ signal M_a	71 445	452 547	255 417	58 683	7273
$\Delta(E-P_z)$ background B_a	4236	41 868	35 711	10 614	1515
Background sources					
Kinematic ambiguities	2019	25 734	24 213	7790	1121
$A_{\pi p}$	(2.6%)	(5.2%)	(8.3%)	(11.2%)	(12.7%)
Other exclusives					
$p\bar{p}$,	47	292	73	<88	<9
M_b	(0.06%)	(0.06%)	(0.8%)	(<2.5%)	(<6.8%)
K^+K^-	473	3318	2410	<1719	<515
M_c	(0.6%)	(0.6%)	(0.8%)	(<2.5%)	(<6.8%)
Mismeasurements	2637	18 171	12 202	2914	411
$(\sum p_\perp)^2$ background N_{mm}	(3.4%)	(3.6%)	(4.2%)	(4.2%)	(4.6%)
$(\sum p_\perp)^2$ signal N_{fm}	73 766	482 344	282 558	67 317	8516
Signal balance	0.3%	0.1%	0.1%	1.2%	1.4%
Background balance	18%	11%	8%	0.8%	1%

The 48 in.×72 in. aperture of this last chamber subtended an angular acceptance of ±230 mrad vertically and ±346 mrad horizontally when measured from the center of the target 104 in. away. (The maximum possible acceptance is for a track passing through the 40 in.×60 in. aperture of the third chamber located 36 in. away from the target: ±507 mrad vertically and ±695 mrad horizontally.)

Details of the performance of the spectrometer are presented elsewhere [10]. We present here some important characteristics relevant to the correlation studies [11]. This spectrometer system achieved single-plane efficiencies of greater than 99%, allowing the efficient reconstruction of events with as many as 20 charged final state particles. The spatial resolution of each plane, when fully optimized, was in the range of 150–200 μm. Particles with momenta between 100 MeV/c and 28 GeV/c were measured with a $\Delta p/p = 0.0016p$ (GeV/c)+0.01. The spectrometer was capable of distinguishing two trajectories that shared common end points in the first and last chambers and were separated by as little as 4 mm in the third and fourth chambers.

The particle momentum measurements are also used to establish that all final state particles are observed and to determine the identity of the final state particles. This is achieved through energy-momentum conservation relations described in detail below. Direct particle identification measurements provide a verification of the kinematically determined particle identities.

There are two detector systems in the apparatus which were used to make direct particle identification measurements: the time-of-flight (TOF) system and the Cherenkov system. The TOF system consisted of two counter hodoscopes: the middle hodoscope (MH) and the rear hodoscope (see Fig. 1). The middle hodoscope consisted of 30 plastic scintillator counters arranged in a picture frame around the "inner aperture" of the spectrometer. The rear hodoscope consisted of 72 counters covering the full downstream aperture of the magnet. Each counter was instrumented with a single photomultiplier tube. The scintillation light detected by each phototube was amplified and the pulse area and arrival time measured by digitizing electronics [12]. This system achieved a 95%
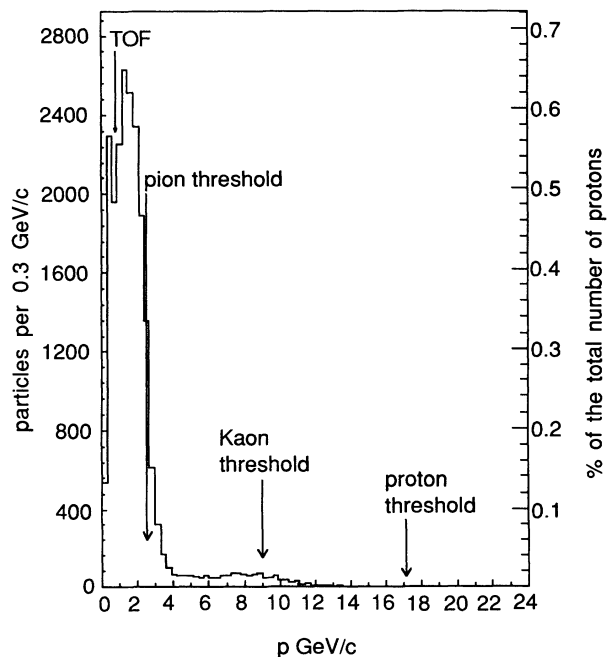

FIG. 6. p_z distribution of positive charged particles whose identity could be either proton or π^+ for reaction (1b).

detection efficiency, with a ±5 pC measurement resolution of the time-integrated signal current and a ±600 ps (standard deviation) arrival time measurement. This provided a π-K separation for particle momenta up to 1 GeV/c, a π-p separation up to 1.6 GeV/c in the rear hodoscope, and a π-p separation up to 0.75 GeV/c in the middle hodoscope.

The Cherenkov counter consisted of 96 cells, divided into 64 small "inner" cells and 32 large "outer" cells, covering the downstream aperture of the magnet. This counter was filled with freon 114 at atmospheric pressure. The operating Cherenkov radiation thresholds for $\pi/K/p$ were 2.55/9.09/17.27 GeV/c. This detector provided high-momentum particle identification. The high segmentation greatly reduced the confusion due to "crowded" particle clusters in high-multiplicity events. The Cherenkov counter phototube pulses were measured with the electronics described previously. The pulse area was used to determine the number of photons emitted as Cherenkov radiation. The pulse arrival time information helped reduce the out-of-time backgrounds due to particle interactions in material surrounding the aperture of the apparatus.

The data acquisition system for this apparatus was designed to trigger and read out events at high rates. The general data-driven architecture [13] allowed for a flexibly configuration trigger. The trigger and data acquisition system are shown in Fig. 2.
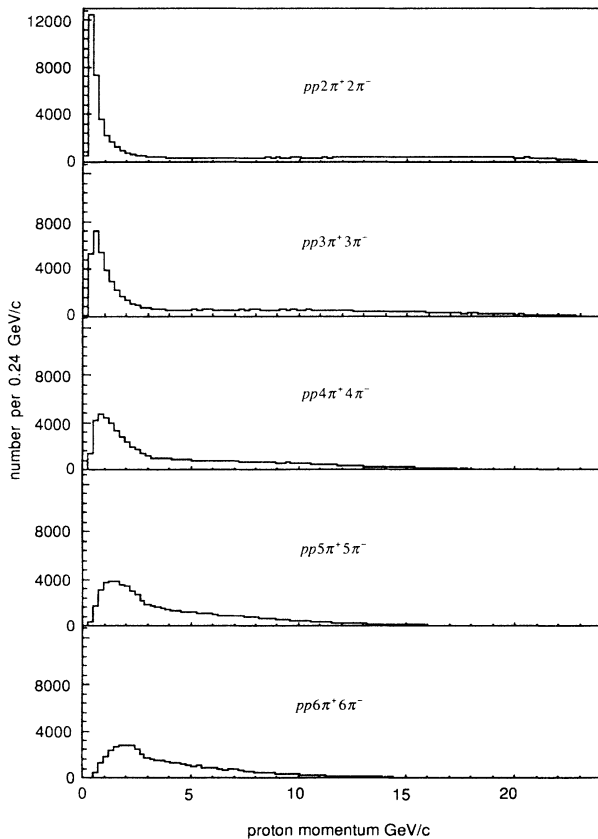
An initial event trigger was indicated by the presence of a scintillator coincidence. This trigger had a built-in dead time of 30 ns. A positive trigger from this coincidence initiated a more complex trigger decision, based on the sum of hodoscope counters with signal above threshold, special counters, or prescale count. These conditions took no more than 60 ns to calculate. A positive decision at this level initiated the digitization of the analog signal information, which had been "stored" by cable delay. The digitization and readout of zero-suppressed data then took an average of 1–2 μs, depending on event size. Once the data were read out, a third decision of whether to keep the data was made using a data-driven processor [14]; this was based on the number of clusters of hit wires in the drift chamber system—effectively a charged-particle multiplicity trigger.

The surviving events were written into buffer memory, and onto tape, at roughly 3000 events per 1.5 s spill. The average event size was 1 kbyte. In a 2 week run, 3×10^8 events were written to 3000 nine-track 6250 bpi tapes.

III. DATA SELECTION

The data sample used in the correlation study have the following characteristics: All final state particles are observed, all events are consistent with the hypothesis that all final state particles originate at a common vertex located within the liquid hydrogen target, and all final state
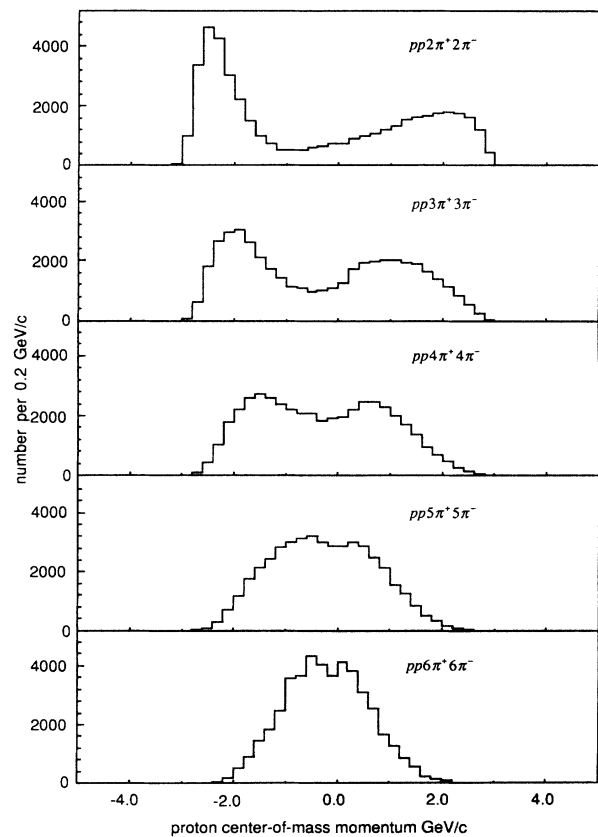

FIG. 7. Proton laboratory p_z momentum distributions for reactions (1a)–(1e).

FIG. 8. Proton center-of-mass p_z momentum distributions for reactions (1a)–(1e).

particles are consistent with the hypothesis that only two are protons and the rest are either π^+ or π^-. The sample selected from the 3×10^8 event data set contains all the candidates for the reactions of the type

$$p + p \to p + p + 2\pi^+ + 2\pi^- \qquad (1a)$$

$$\to p + p + 3\pi^+ + 3\pi^- \qquad (1b)$$

$$\to p + p + 4\pi^+ + 4\pi^- \qquad (1c)$$

$$\to p + p + 5\pi^+ + 5\pi^- \qquad (1d)$$

$$\to p + p + 6\pi^+ + 6\pi^- \; . \qquad (1e)$$

Reactions with fewer than six charged particles were rejected by the multiplicity trigger. (Note that reactions with two- and four-particle final states cannot have two identical charged pions.) Reactions with greater multiplicity than 14 charged particles do not occur in the data with sufficient frequency to allow a statistically significant analysis to be performed. Table I summarizes the numbers of events in the samples for reactions (1a)–(1e).

The data selection is performed in four analysis steps. At the first step, the raw drift chamber data are used to reconstruct the trajectories of the charged particles through the magnetic field. This step is executed by a special purpose computer [14], the "hardware processor," with programmable selection criteria. Events are selected if either (1) there is a reconstructed charge multiplicity of greater than 11 tracks or (2) the sum of the reconstructed track, longitudinal momenta for the event is within ± 5 GeV/c of the beam momentum (27.5 GeV/c). In both cases, tracks with longitudinal momentum greater than 24 GeV/c were excluded (this allows events with multiple beam protons, where only one of the protons interact in the target). Roughly 50% of the sample survives these criteria.

The second reconstruction step finds any remaining trajectories and the vertices formed by the intersection of the tracks. This process begins by attempting to assign any unassigned wire "hits" to existing track trajectories. Those wire hits which remain unassigned are used to form additional candidate track trajectories. Once all trajectories are determined within the constraints of the pattern recognition algorithm, the intersections of these track trajectories are established. The determination of the primary vertex where the interaction occurred provides an additional space point which is used along with the drift chamber information to determine the track trajectories more precisely. Secondary vertices which occur downstream of the primary vertex are tested to determine if their identity is consistent with known long-lived particles (e.g., K_S^0 or Λ^0). For the purpose of the correlation study, only those events which are candidates for full event reconstruction are selected (the selection criteria are described below). The fraction of the data which survives reconstruction at this stage is 10%.

At the third step of the event reconstruction, the incident beam particle trajectory and momenta are calculated. Kinematic constraints and conservation laws are imposed to obtain particle identification. The direct particle identification information is used to eliminate inconsistent assignments.
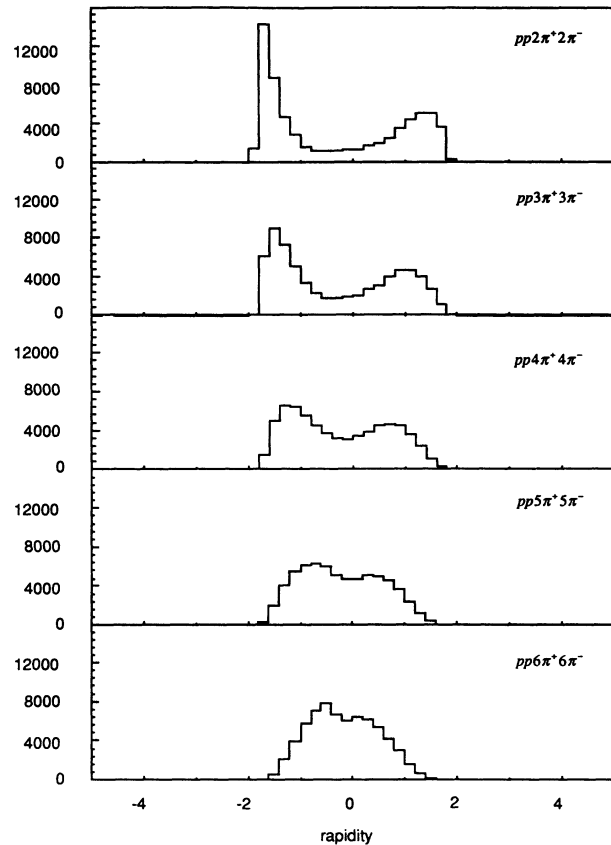

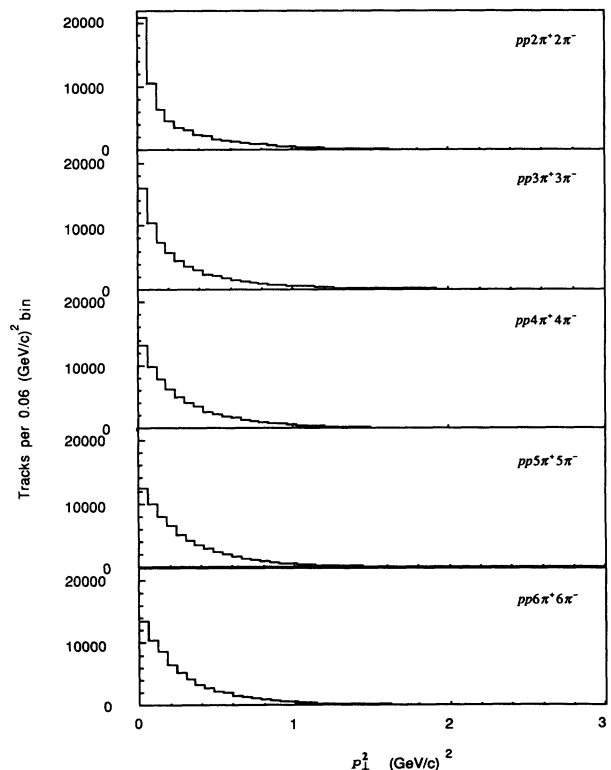FIG. 9. Proton rapidity distributions for reactions (1a)–(1e).

FIG. 10. Proton transverse momentum squared distributions for reactions (1a)–(1e).

The fourth and final step of the analysis uses the events surviving the three reconstruction steps and various selection criteria. These criteria are used to isolate candidate events corresponding to reactions (1a)–(1e).

It is important to demonstrate that the final data samples are free from background. We provide here more detail on the methods and effectiveness of the selection criteria. The kinematic constraints are applied in three cuts. The first cut requires that the square of the sum of final state particle momenta vectors perpendicular to the initial beam direction be consistent with the detector resolution. Figure 3 shows the distribution of the square of the sum of $\mathbf{p}_\perp$ for the events used in this study. Note the relatively flat distribution of events at large $(\sum \mathbf{p}_\perp)^2$. This is indicative of events with missing final state particles, with mismeasured beam momentum or with mismeasured final state particles. The peak at small $(\sum \mathbf{p}_\perp)^2$ is due to events in which all final state particles have been measured. The width of this peak is $\sim (40$ MeV/$c)^2$, consistent with Monte Carlo studies of the spectrometer's resolution. Events in this sample were required to have a $(\sum \mathbf{p}_\perp)^2$ less than or equal to 0.0016 $(\text{GeV}/c)^2$.

The conservation of longitudinal momentum (along the z axis) forms the second cut. The difference of the beam momentum (measured by the beam spectrometer) and the sum of the momenta of the final state particles (measured by the spectrometer) is shown in Fig. 4. The cut requires the momentum difference to be less than ± 1 GeV/c. Since the standard deviation of the distribution in Fig. 4 is 300 MeV/c, it is a relatively loose cut.

In the third cut, the energy balance constraint is used to assign particle identities to the final state particles. Since low-momentum tracks are measured more precisely than the high-momentum tracks, energy conservation is not used directly. Instead, the sum of the energy minus the z momentum is calculated for the initial and final states. We use the relationship

$$E_i^2 = m_i^2 + p_{\perp i}^2 + p_{zi}^2 \ ,$$

where E_i, m_i, $p_{\perp i}$, and p_{zi} are the energy, mass, transverse momentum, and z component of the momentum for the ith particle.

This relationship can be rearranged as

$$E_i - p_{zi} = \frac{m_i^2 + p_{\perp i}^2}{E_i + p_{zi}} \ . \tag{2}$$

Since the sum of E_i and p_{zi} are each individually conserved between the initial and final states, their difference is conserved. Using expression (2) eliminates the correlated error between E_i and p_{zi}. Figure 5 shows the distri-
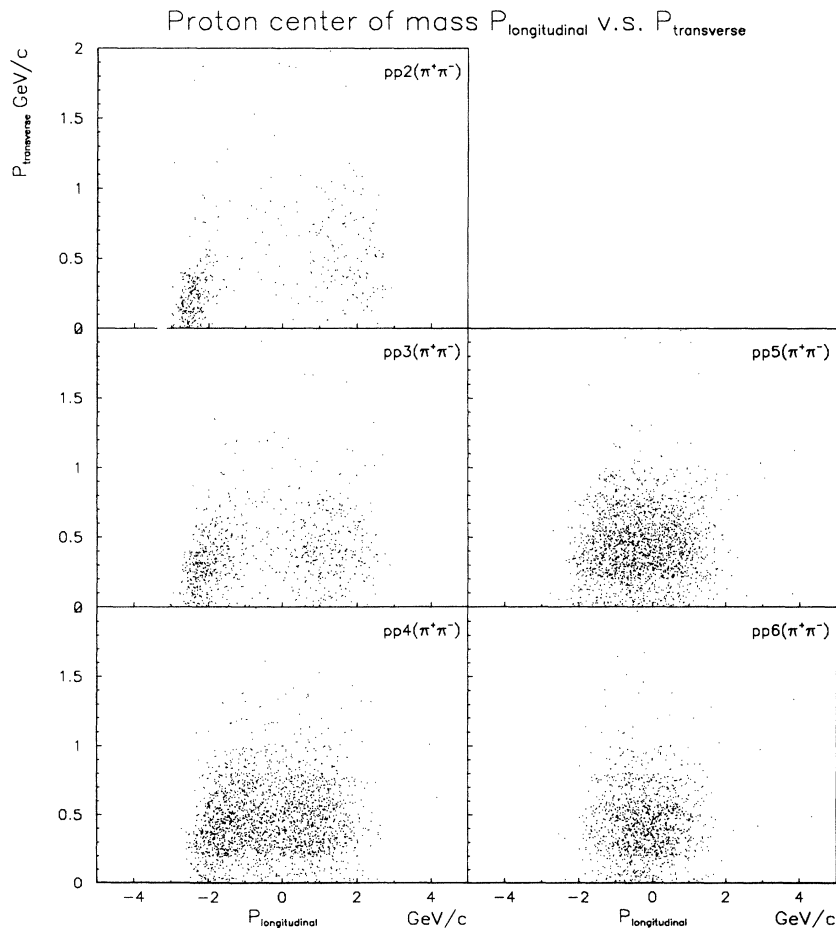

FIG. 11. $p_\text{longitudinal}$ vs $p_\text{transverse}$ for protons in reactions (1a)–(1e).

butions for the difference of the sums from initial to final states:

$$\Delta(E - p_z) \equiv \sum_{\text{initial}} \frac{m_i + p_{1i}^2}{E_i + p_{zi}} - \sum_{\text{final}} \frac{m_j^2 + p_{1j}^2}{E_j + p_{zj}} \ . \quad (3)$$

The fully reconstructed events have a $\Delta(E - p_z)$ distribution width of 4 MeV. The displacement of the distribution from zero probably results from small coordinate misalignments in the spectrometer. Note that expression (3) can be used to assign the final state particle identities by requiring that the masses m_j are selected to minimize $\Delta(E - p_z)$.

In addition to the kinematic constraints, only final states which satisfy the additive conservation laws (e.g., charge, strangeness, charm, baryon number, etc.) are considered. The effect of these cuts on the data sample are summarized in Table I.

The level of backgrounds can be estimated for the isolated reactions (1a)–(1e) and are shown in Table II. The nature of backgrounds falls into three major categories: missing particles, incorrect identification of topology, and incorrect assignment of particle identity within topology. The first category, missing particles, can occur when these particles have sufficiently low mass and momenta that they cannot be distinguished from momentum mea-

surement variations due to the spectrometer resolution. In particular, π^0's dominate these backgrounds.

The second background category, incorrect identification of topology, is due to kinematic ambiguities unresolved by the direct particle identification measurements. For instance, a $\pi^+\pi^-$ pair substituted for a K^+K^- pair may give a $\Delta(E - p_z)$ value within cut limits for both assumptions. If no additional information is available to determine the identity of these particles, the $\pi^+\pi^-$ solution is assumed to be correct.

The third category, incorrect assignment of particle identity within topology, occurs when the assignment of particle identity is ambiguous. For example, if the z momentum for the two tracks is large, then the $\Delta(E - p_z)$ will remain the same (within resolution), independent of the assignment of masses to these tracks. The possible identity of these tracks is ambiguous, and two solutions exist for the event. If no direct particle identification measurements are available to resolve the ambiguity, either assignment is possible. Figure 6 shows the momentum distribution for particles whose identity is ambiguous between π^+ or p. As indicated in Fig. 6, using the TOF system to distinguish π^+ and p reduces the number of events with π^+-p ambiguities in the particle momentum region below 1 GeV/c. The Cherenkov measurement resolves the ambiguity for particle momenta above
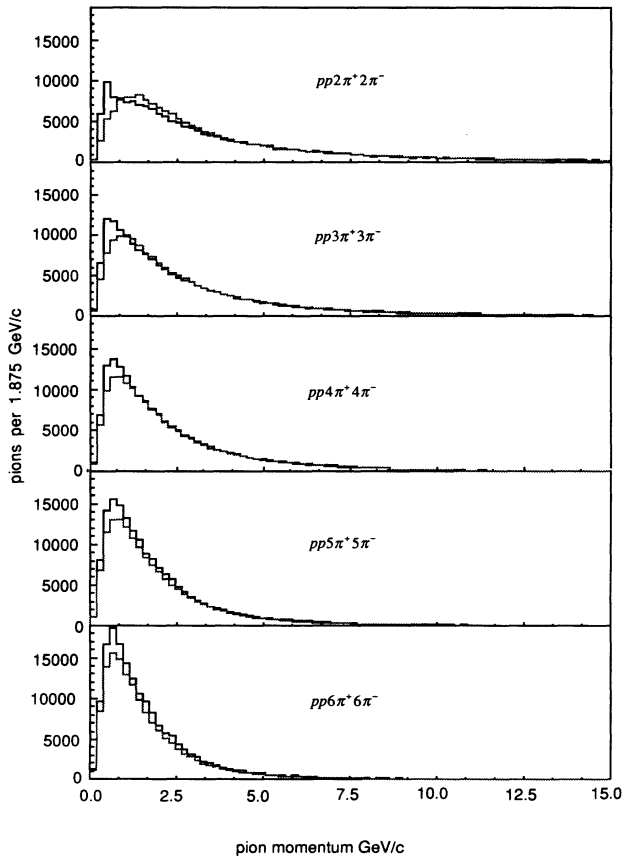

FIG. 12. π^+ (solid line) and π^- (shaded line) laboratory frame longitudinal momentum distributions for reactions (1a)–(1e).
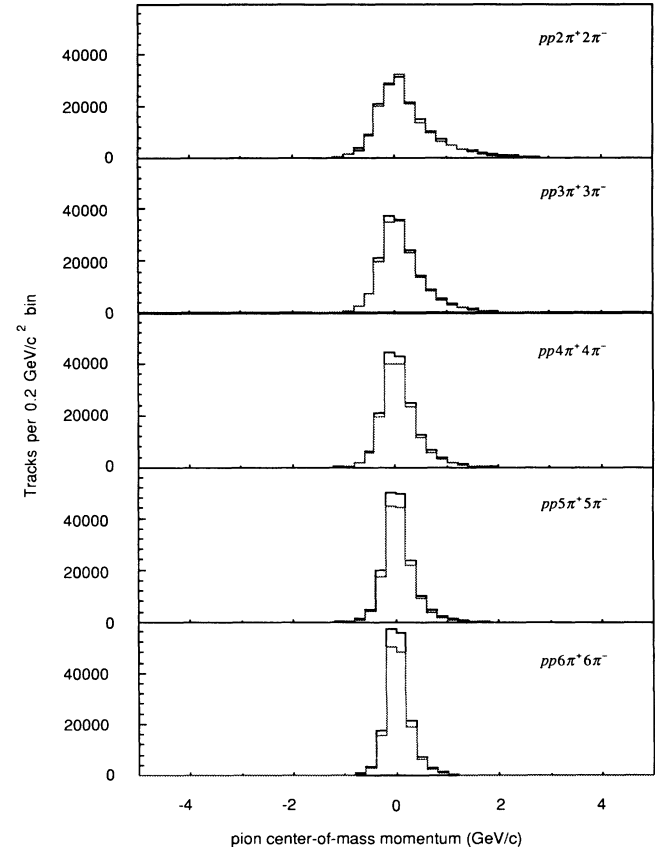

FIG. 13. π^+ (solid line) and π^- (shaded line) center-of-mass longitudinal momentum distributions for reactions (1a)–(1e).

2.5 GeV/c. The events used in the pion correlation studies contain equal numbers of π^+ and π^-. The π^- cannot be confused with any other particle in the event. All negative particles are pions. The comparison of the π^+ and π^- distributions helps to determine the effect that the ambiguous p-π^+ identification has on the π^+ distributions.

The background estimates presented in Table II are calculated by accounting for all of the fully reconstructed events. This is done for each topology separately. The total number of fully reconstructed events, N_{fm}, is determined by a fit to the $(\Sigma\mathbf{p}_\perp)^2$ distribution (Fig. 3). (The fit function, determined empirically, is the sum of two exponential distributions and a linear polynomial, describing the signal and background, respectively.) This fit also provides the number of events with missing particles or mismeasured particles, N_{mm}. The sum of these two numbers equals the number of events in the topology:

$$N = N_{fm} + N_{mm} .$$

The total number of fully reconstructed events can be calculated by summing the number of events for each fully reconstructed topology. This number is determined by fitting the $\Delta(E - P_z)$ distribution for each topology (Fig. 5):
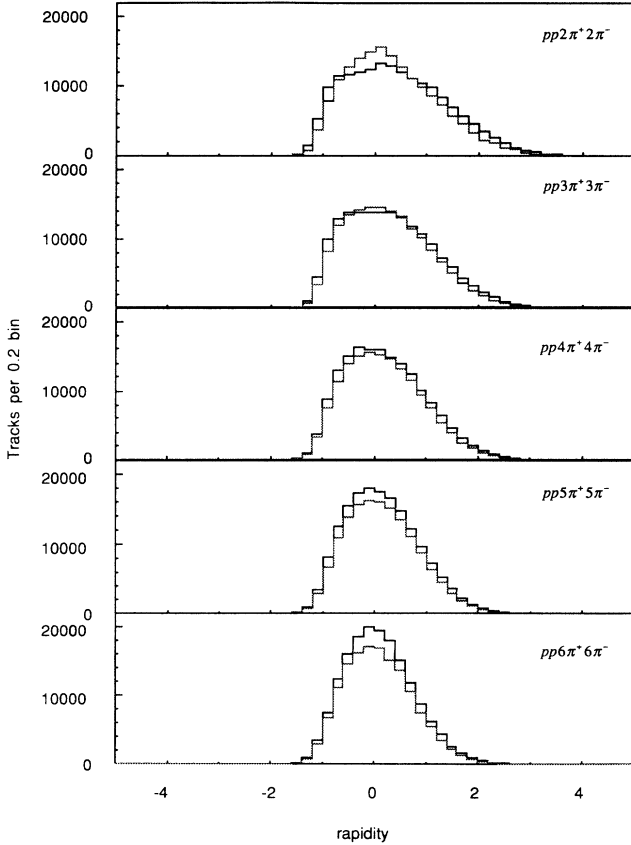
$$N_{fm} = M_a + M_b + M_c + \cdots ,$$

where M_a is the number of fully reconstructed events for topology a, M_b for b, etc. (The fit function used here is the sum of two Gaussian distributions and a quadratic polynomial, describing the signal and background, respectively.) For the topologies corresponding to reactions (1a)–(1e), the dominant fully reconstructed backgrounds are those for which a $\pi^+\pi^-$ pair is replaced by a K^+K^- or $p\bar{p}$ pair. The fits to the topologies which include K^+K^- and $p\bar{p}$ pairs provide the number of these events which are backgrounds to the associated $\pi^+\pi^-$ topologies. For the topologies corresponding to reactions (1a)–(1e), we would write

$$B = M_{KK} + M_{p\bar{p}} + N_{mm} + A_{\pi p} ,$$

where B is the background, $M_{KK}, M_{p\bar{p}}$ are the number of fully reconstructed events with K^+K^- and $p\bar{p}$ pairs replacing $\pi^+\pi^-$ pairs, and $A_{\pi p}$ is the number of events with π^+-p ambiguities for the topology. For a given topology, we also have the relation

$$N = M_a + B_a ,$$

where B_a is also determined in the $\Delta(E - p_z)$ fit which determines M_a.

Table II lists these quantities obtained by fits for the five topologies studied. In all cases the sum of individual background "components" exceeds the background
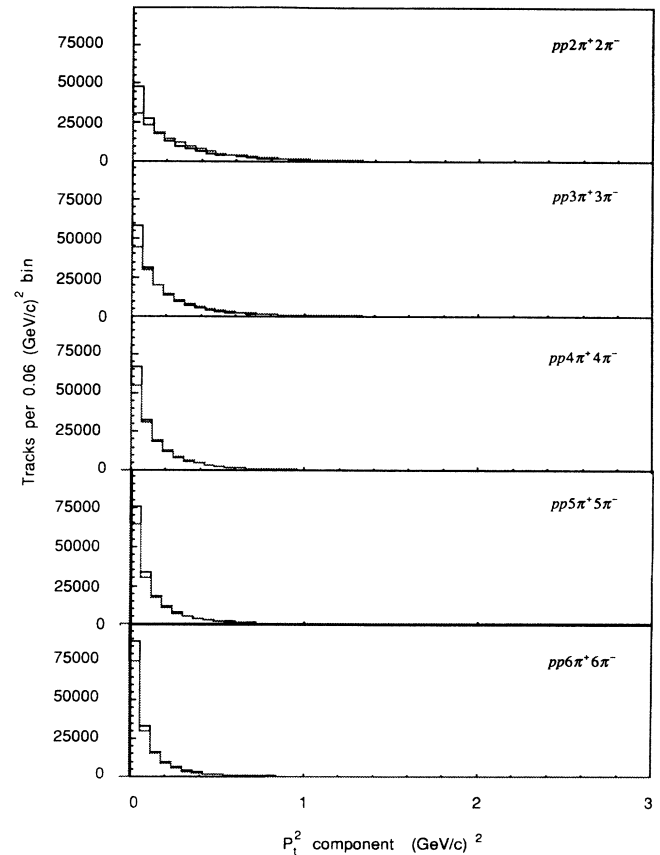

FIG. 14. π^+ (solid line) and π^- (shaded line) rapidity distributions for reactions (1a)–(1e).

FIG. 15. π^+ (solid line) and π^- (shaded line) transverse momentum distributions for reactions (1a)–(1e).

determined by the fits of $\Delta(E - p_z)$. This is because the background categories are not exclusive. Note that for all topologies except the six-track topology, the dominant background contribution is from π^+-p ambiguities. The worst topology, 16 track, has a 17% background for π^+. All topologies have less than 5% backgrounds for π^-. Note also that the number of fully reconstructed events, determined by a direct fit $(\sum\mathbf{p}_\perp)^2$, agrees well with the sum of fully reconstructed events found for each topology as determined by fits to $\Delta(E - p_z)$.

IV. DATA ANALYSIS

A. Production characteristics

Reactions (1a)–(1e) have production characteristics which vary with multiplicity as a result of both kinematic and dynamic effects. Knowledge of these production characteristics is essential because they determine the particle momenta distributions. The correlations caused by kinematics, as revealed in the particle momentum distributions, must be distinguished from correlations caused by dynamics and by the statistics obeyed by the particles.

Our description of the production characteristics is based on the single-particle momentum distributions for each reaction (1a)–(1e). Figure 7 shows the laboratory momentum distributions for protons in these reactions. The selection criteria at the first reconstruction stage reduce the acceptance for high-momentum protons. The low-momentum cutoff is due to the finite backward (in the center-of-mass frame) acceptance of the spectrometer and the requirement that the entire event be observed. The proton momentum distributions in the interaction's center-of-mass frame are shown in Fig. 8. It is readily apparent that for the low-multiplicity reactions, the protons are isolated from each other. As the multiplicity increases, the proton momentum distributions are less isolated. This is an effect which cannot be explained solely by the commensurate decrease in the available kinetic energy. [The maximum center-of-mass momentum for the proton ranges from 3.5 GeV/c for reaction (1a) to 3.2 GeV/c for reaction (1e).] The proton rapidity distribution is shown in Fig. 9. The proton $p_\perp^2$ distribution shown in Fig. 10 also appears to be multiplicity dependent, since lower multiplicities have smaller $p_\perp^2$ than larger multiplicities. The plot of center-of-mass $p_{\text{transverse}}$ vs $p_{\text{longitudinal}}$ in Fig. 11 shows that some kinematic isolation of the protons persists at low $p_\perp^2$ to moderate multiplicities. Taken together, these distributions indicate that several production mechanisms may be important in describing the reactions (1a)–(1e). Among these are diffractive production
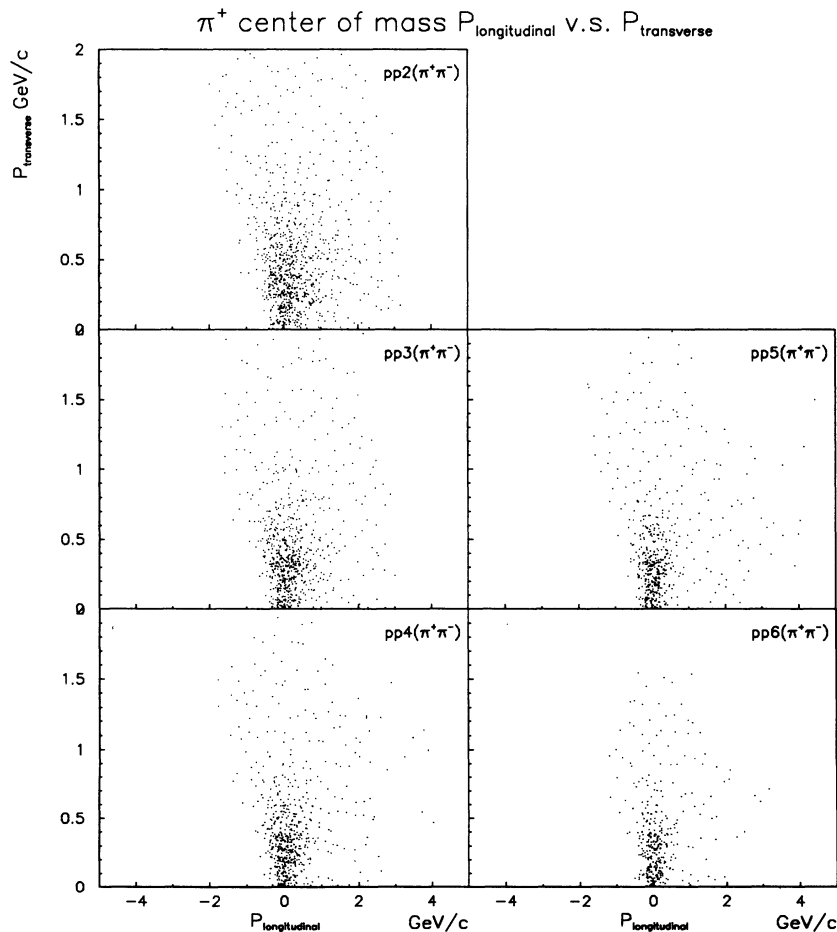

FIG. 16. $p_{\text{longitudinal}}$ vs $p_{\text{transverse}}$ for π^+ in the reactions (1a)–(1e).

(see Ref. [10]), peripheral production, and some form of central production (e.g., longitudinal phase space). The relative proportion of these production mechanisms may also change as a function of multiplicity (see Ref. [10]).

The π^+ and π^- laboratory momentum distributions are shown in Fig. 12. The differences between the π^+ and π^- distributions are pronounced at low laboratory momentum. At low momentum, there is a high probability of confusing the p and π^+ and there is a large Δ^{++} production cross section for these reactions. The $\Delta^{++} \rightarrow p\pi^+$ decay tends to be a source of soft pions since the Δ^{++} decay kinematics require that the proton receive much of the Δ^{++} momentum.

The momentum distributions in the interaction center-of-mass frame (Fig. 13) for the π^+ and π^- indicate that the pions are produced with small momenta in the center of mass. The distributions have asymmetric tails because of the finite backward acceptance of the spectrometer.

Both the center-of-mass momentum distributions and the rapidity distribution (Fig. 14) narrow as the multiplicity of the reaction increases. This effect is at least partly due to kinematics: Less energy is available to individual pions as the number of pions increases. The $p_\perp^2$ distributions for the pions are shown in Fig. 15. It will be seen later that the Monte Carlo–generated events for reac-

tions (1a)–(1e) which contain no dynamics have the same qualitative behavior. From the Monte Carlo results, we infer that these multiplicity dependences are at least partly due to kinematics.

The plots of center-of-mass $p_{\text{transverse}}$ vs $p_{\text{longitudinal}}$ (Figs. 16 and 17) show the effect of the geometric acceptance on backward pions, as well as the decreasing kinematic range, as the multiplicities increase.

B. Correlations

The experimental signature of pion correlations due to Bose-Einstein statistics (referred to as Bose-Einstein correlations) is an increased probability of finding two identical particles with the same momenta. The range of relative momenta for which the probability is enhanced is related to the space-time separation of the particle sources. However, the actual distribution of the relative momenta of two identical particles can be influenced by both kinematic and dynamic phenomena. Both strong and electromagnetic final state interactions can play significant roles. In most cases direct calculations of the distribution shapes are not possible.

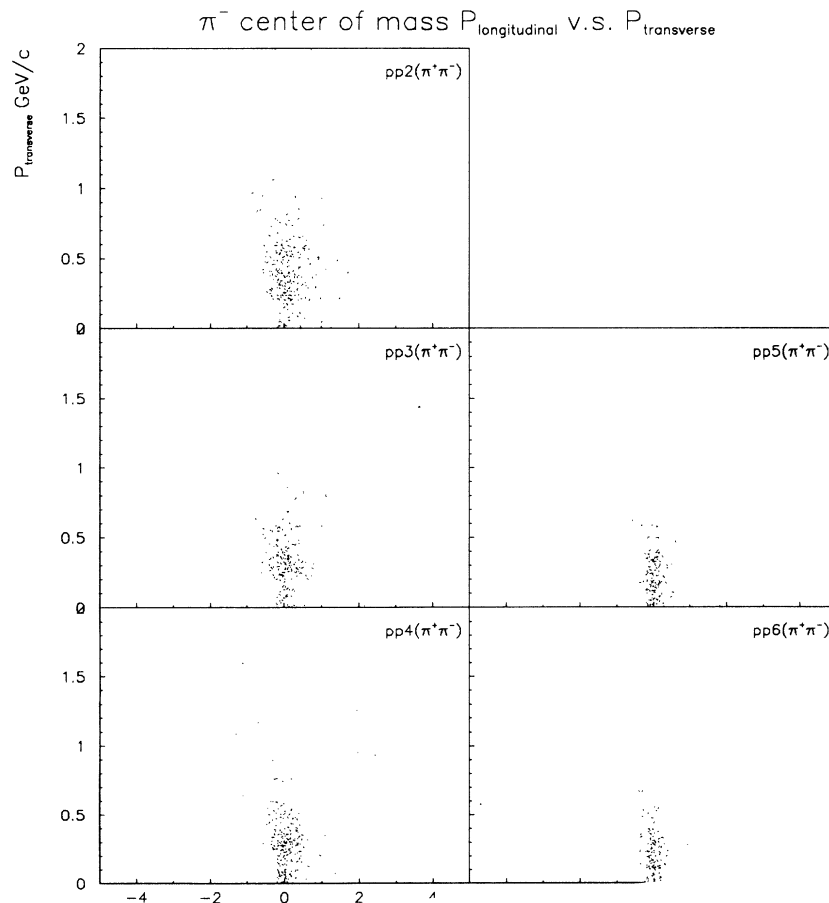Correlation analyses [6] usually assume that indepen-

FIG. 17. $p_{\text{longitudinal}}$ vs $p_{\text{transverse}}$ for π^- in the reactions (1a)–(1e).

dent sources of equal strength are described by a Gaussian distribution in space *and* time. This model of two-particle production harks back to the original GGLP model, however inappropriate the original statistical model has become for describing particle production. Until better theoretical guidance is forthcoming, these parametrizations provide a way of organizing the existing data.

We define the relative four-momentum squared of two pions:

$$Q^2 = -(P_1 - P_2)^2$$
$$= M_{12}^2 - 4m_\pi^2$$
$$= -(2m_\pi^2 - 2E_1 E_2 + 2p_1 p_2 \cos\vartheta_{12}) ,$$

where P_1 and P_2 are the four-momenta of pions 1 and 2, M_{12} is the invariant mass of particles 1 and 2, m_π is the pion mass, and E_1, E_2 and p_1, p_2 are the energies and momenta of pions 1 and 2, respectively.

The Q^2 distributions for two like-sign pions for the reactions (1a)–(1e) of this data sample ($\pi^+\pi^+$, solid line, and $\pi^-\pi^-$, dotted line) are shown in Fig. 18. The width of the Q^2 distributions is decreasing with increasing multiplicity. As we will show later, the Monte Carlo Q^2 dis-

tributions using a generator without dynamics display a qualitatively similar behavior.[ ] We infer that this dependence is primarily a kinematic effect, as we observed previously in the single-particle longitudinal momentum distributions.

The data distribution must now be compared to a distribution lacking any Bose-Einstein correlation. Ideally, such a comparison distribution should contain *all other physics*. The ratio of the data to the comparison distribution provides the "correlation function," which is the Fourier-transformed source distribution. The validity of this procedure and the physical interpretation of the resulting parametrizations will be taken up in another paper [15]. The distribution ratios can be parametrized in the form

$$R(Q^2) = 1 + \alpha e^{\beta Q^2} ,$$

where the ratio is unity at large Q^2 and $1+\alpha$ at small Q^2. In the original GGLP paper, α was unity and β was related to the inverse square of the reaction volume radius.

The creation of the comparison distribution is a central problem for all analyses of Bose-Einstein correlations. In this study, the use of fully reconstructed events poses additional constraints. These constraints originate from the need to calculate the effects of geometric acceptance and
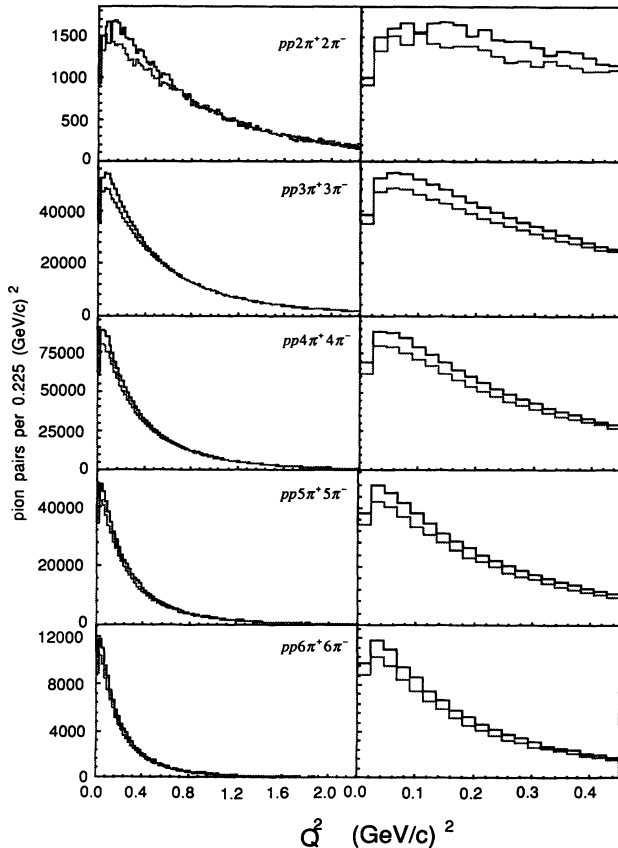

FIG. 18. $\pi^+\pi^+$ and $\pi^-\pi^-$ Q^2 distributions for reactions (1a)–(1e); the column on the right has an expanded scale at small Q^2.
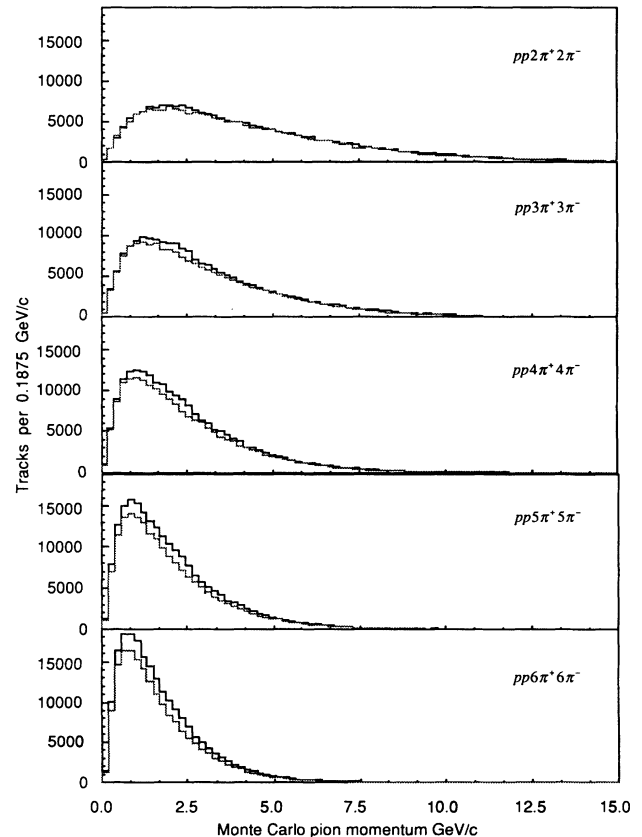
FIG. 19. π^+ (solid line) and π^- (shaded line) laboratory frame longitudinal momentum distributions for reactions (1a)–(1e) generated by a LIPS Monte Carlo simulation.

reconstruction efficiencies on the comparison samples. Thus the comparison sample should be generated with the correct dynamics, with the proper kinematic effects, but lacking the pion correlations. This daunting task is not currently achievable from fundamental principles or from empirical models of particle reactions at these energies. Instead of developing an empirical model whose applicability might be limited and whose validity might be difficult to affirm, we propose an ansatz to the standard parametrization. We use as a comparison distribution Lorentz-invariant phase space. We further assume that the standard correlation function is modulated by a "source function":

$$R(Q^2)=(1+\alpha e^{\beta Q^2})S(Q^2) ,$$

where $S(Q^2)$ contains the large Q^2 behavior of the distributions, presumably related to the dynamics of pion production.

There is no known theoretical argument that suggests the separability of the correlation and source functions or the form of the source function. However, other experiments [16] that have required more complex parametrizations of the correlation function use parametrizations that resemble those of our ansatz.
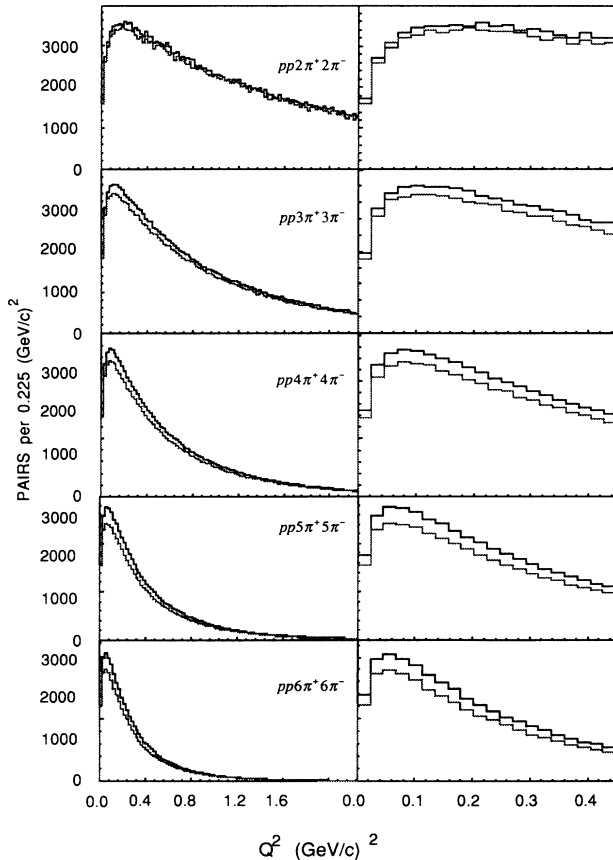
C. Comparisons to LIPS

Our comparison sample is generated using Lorentz-invariant phase space. Events for each of the reactions (1a)–(1e) are produced with a uniform density in their respective phase space volumes. The events are unconstrained in angular momentum. The generator model assumes a pointlike interaction of spinless particles and produces pointlike spinless particles. We assume that the effects of spin and angular momentum in reactions (1a)–(1e) average to the spinless case. These events are passed through a detector simulation program which produces data in the format of real events. The analysis of these simulated events then follows the procedures used to analyze the real events.

The resulting π^+ (solid line) and π^- (dotted line) longitudinal momentum distributions are shown for each reaction (1a)–(1e) in Fig. 19. The multiplicity dependence of these distributions is similar to that seen in the data (Fig. 12). Because the dominant dynamical effect of pion production at these energies is the limiting of transverse momentum scale of the produced particles, the major difference between the LIPS and data is the difference in the transverse momentum distribution. This will cause the LIPS-generated events to have a narrower distribution in longitudinal momentum. The LIPS-generated events show the same increase in the number of π^+ to π^-

FIG. 20. $\pi^+\pi^+$ (solid line) and $\pi^-\pi^-$; (shaded line) Q^2 distributions for reactions (1a)–(1e) generated by a LIPS Monte Carlo simulation; the column on the right has an expanded scale at small Q^2.
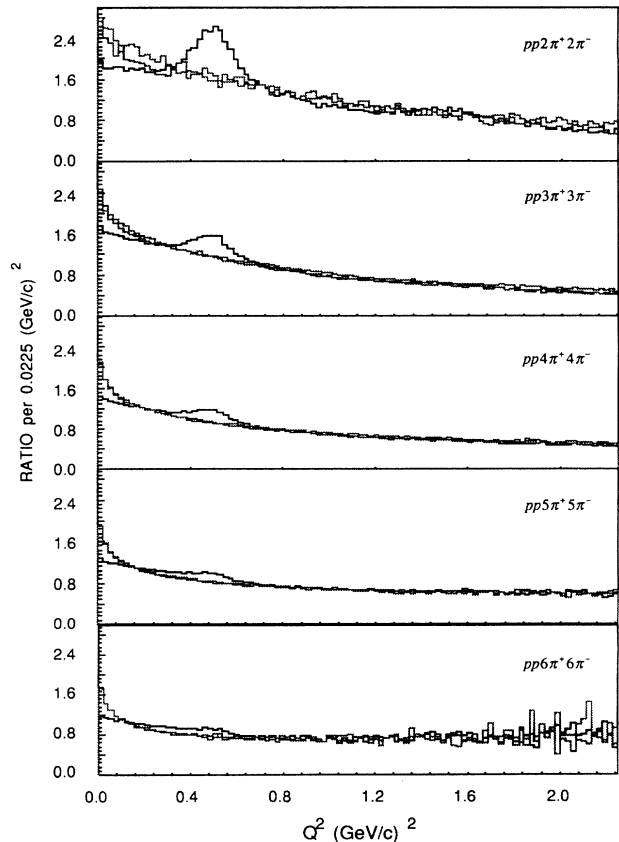

FIG. 21. Ratio of $\pi^+\pi^+$ (shaded line), $\pi^-\pi^-$ (shaded line), and $\pi^+\pi^-$ (solid line), Q^2 distributions data-to-LIPS Monte Carlo simulation for reactions (1a)–(1e).

TABLE III. Parameter values for function (4), Gaussian correlation, fit to $\pi^+\pi^+$ Q^2 ratios for reactions (1a)–(1e).

Gaussian parameter	pp $2\pi^+2\pi^-$	pp $3\pi^+3\pi^-$	pp $4\pi^+4\pi^-$	pp $5\pi^+5\pi^-$	pp $6\pi^+6\pi^-$
α	0.152	0.333	0.453	0.451	0.189
	±0.113	±0.021	±0.015	±0.021	±0.053
β	−34.590	−22.550	−24.580	−26.160	−51.570
	±37.760	±2.119	±1.321	±1.811	±29.770
γ	22.600	10.180	3.125	1.521	1.414
	±10.230	±0.521	±0.045	±0.026	±0.109
δ	1.893	1.360	0.978	0.583	0.198
	±0.123	±0.032	±0.024	±0.030	±0.024
λ	0.109	0.176	0.382	0.559	0.684
	±0.049	±0.009	±0.006	±0.007	±0.009
χ^2/N_{DF}	111.9/95	128.4/95	99.2/95	106.1/95	125.6/95

TABLE IV. Parameter values for function (5), Bowler correlation, fit to $\pi^+\pi^+$ Q^2 ratios for reactions (1a)–(1e).

Bowler parameter	pp $2\pi^+2\pi^-$	pp $3\pi^+3\pi-$	Final state pp $4\pi^+4\pi^-$	pp $5\pi^+5\pi^-$	pp $6\pi^+6\pi^-$
α	1.669	0.431	0.601	0.645	0.257
	±20.790	±0.029	±0.020	±0.036	±0.205
β	0.004	0.061	0.061	0.066	0.035
	±0.028	±0.009	±0.005	±0.007	±0.045
γ	22.480	10.860	3.064	1.329	1.308
	±10.450	±0.692	±0.052	±0.044	±0.382
δ	1.884	1.443	1.098	0.709	0.209
	±0.128	±0.043	±0.038	±0.056	±0.071
λ	0.110	0.161	0.367	0.549	0.683
	±0.050	±0.011	±0.007	±0.008	±0.012
χ^2/N_{DF}	113.3/95	120.7/95	87.8/95	105.2/95	126.5/95

TABLE V. Parameter values for function (4), Gaussian correlation, fit to $\pi^-\pi^-$ Q^2 ratios for reactions (1a)–(1e).

Gaussian parameter	pp $2\pi^+2\pi^-$	pp $3\pi^+3\pi^-$	pp $4\pi^+4\pi^-$	pp $5\pi^+5\pi^-$	pp $6\pi^+6\pi^-$
α	0.343	0.439	0.533	0.553	0.321
	±0.077	±0.023	±0.015	±0.022	±0.057
β	−24.030	−24.190	−19.910	−25.140	−42.970
	±7.564	±1.837	±0.905	±1.445	±12.930
γ	25.160	9.062	2.983	1.472	1.294
	±27.580	±0.673	±0.078	±0.026	±0.091
δ	2.731	1.724	1.332	0.714	0.266
	±0.312	±0.049	±0.045	±0.040	±0.036
λ	0.083	0.179	0.363	0.548	0.664
	±0.093	±0.013	±0.009	±0.008	±0.012
χ^2/N_{DF}	104.6/95	113.5/95	123.2/95	88.1/95	76.6/95

TABLE VI. Parameter values for function (5), Bowler correlation, fit to $\pi^-\pi^-$ Q^2 ratios for reactions (1a)–(1e).

Bowler parameter	$pp \ 2\pi^+2\pi^-$	$pp \ 3\pi^+3\pi^-$	Final state $pp \ 4\pi^+4\pi^-$	$pp \ 5\pi^+5\pi^-$	$pp \ 6\pi^+6\pi^-$
α	0.473	0.577	0.715	0.795	0.465
	±0.186	±0.037	±0.021	±0.035	±0.096
β	0.034	0.050	0.079	0.068	0.037
	±0.022	±0.006	±0.006	±0.006	±0.022
γ	12.540	9.645	3.069	1.295	1.153
	±6.899	±0.870	±0.118	±0.036	±0.191
δ	2.500	1.819	1.614	0.941	0.295
	±0.301	±0.063	±0.080	±0.083	±0.065
λ	0.161	0.165	0.330	0.527	0.662
	±0.086	±0.015	±0.013	±0.012	±0.013
χ^2/N_{DF}	112.4/95	113.5/95	109.8/95	80.2/95	77.2/95

with multiplicity, as was observed in the data. This increase is due to background from π^+-proton ambiguity.

The π^+ distribution does not agree with the LIPS generator at low momentum (0.5 GeV/c). This is due to π^+ particles which are decay remnants of low-momentum Δ^{++} production. The LIPS generator contains no resonances and thus does not reproduce the kinematics for all π^+ found in the data in this momentum range.

Figure 20 shows the two-pion Q^2 distributions for the LIPS-generated data. Here the narrowing of the distributions with increasing multiplicity is purely kinematic. Both these distributions and the data (Fig. 18) are the result of an identical analysis procedure. The bin-by-bin ratio of these distributions is shown in Fig. 21, where "like-sign" pair distribution ratios ($\pi^+\pi^+$, shaded line, and $\pi^-\pi^-$, dotted line) are compared with the "unlike-
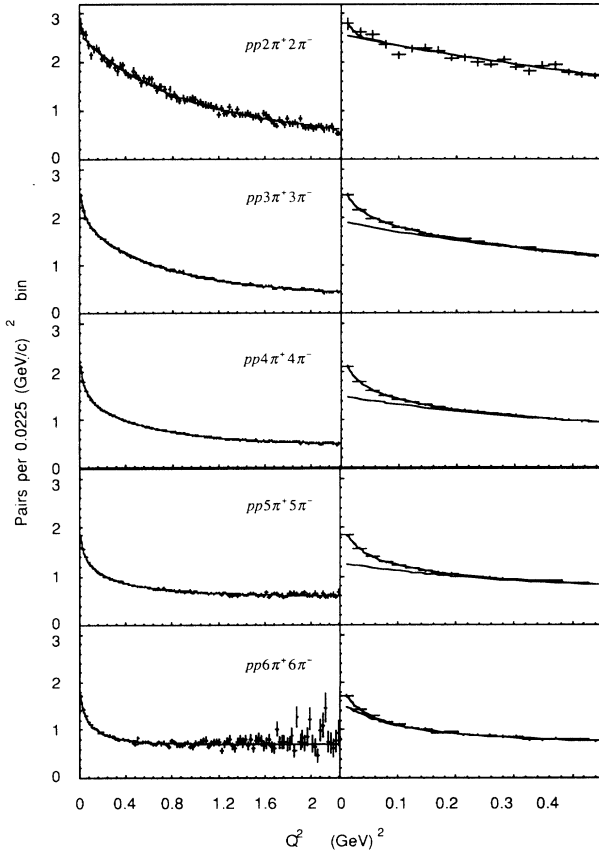

FIG. 22. $\pi^+\pi^+$ Q^2 ratios with fit of function (4), Gaussian correlation, superimposed for reactions (1a)–(1e). Plots on right show low Q^2 region expanded; the lower curve is the source function.
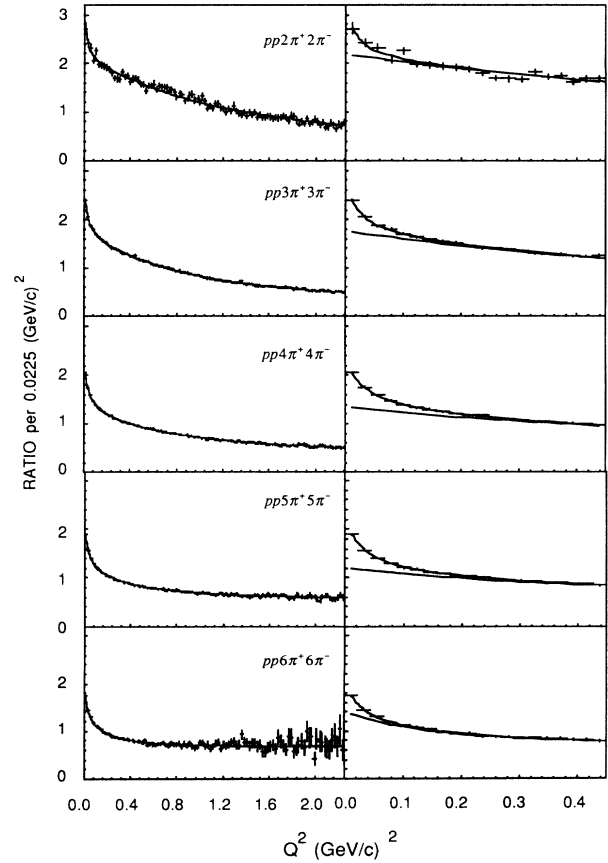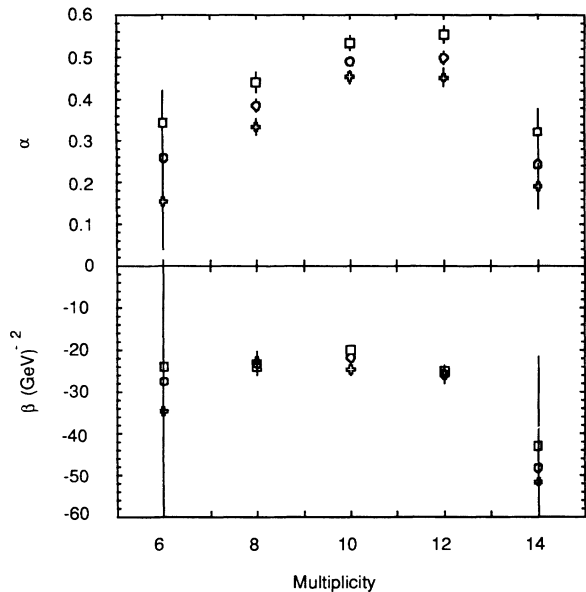

FIG. 23. $\pi^-\pi^-$ Q^2 ratio with fit of function (4), Gaussian correlation, superimposed for reactions (1a)–(1e). Plots on right show low Q^2 region expanded; the lower fit curve is the "source function."

FIG. 24. α (upper) and β (lower) parameters from fits of function (4), Gaussian correlation, to $\pi^+\pi^+$ (box) and $\pi^-\pi^-$ (cross) Q^2 ratios for reactions (1a)–(1e). The $\pi^+\pi^+,\pi^-\pi^-$ combined are indicated by the circle.

sign" (solid line) pair ratios. The distribution ratios for each topology are area normalized to each other for ease of comparison.

The Q^2 resolution can be estimated from Monte Carlo simulations by calculating Q^2 for both the generated pion pairs and for the reconstructed pion pairs. The difference is largest for small Q^2 due to both momentum resolution and the pair opening angle resolution. The difference divided by the generated value is found to be
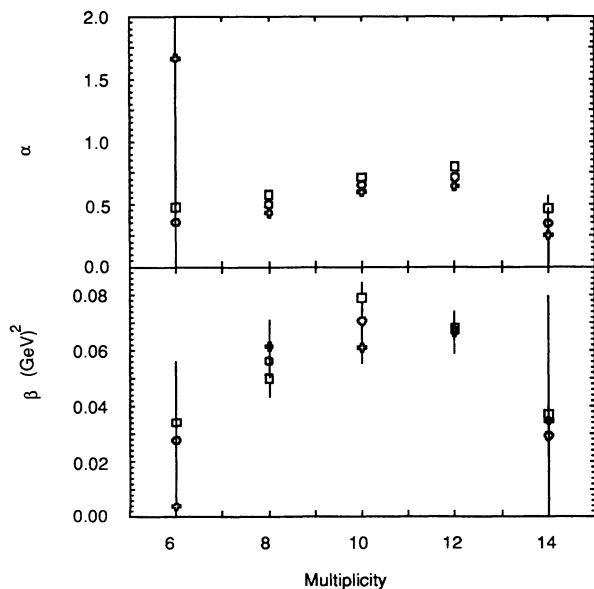

FIG. 25. α (upper) and β (lower) parameters from fits of function (5), Bowler correlation, to $\pi^+\pi^+$ and $\pi^-\pi^-$ Q^2 ratios vs final state multiplicity. The $\pi^+\pi^+,\pi^-\pi^-$ combined are indicated by the circle.
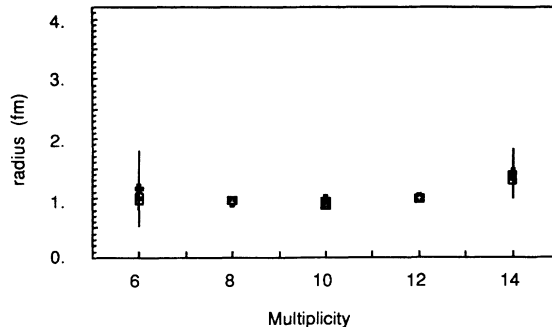

FIG. 26. Interaction volume radius from fits of function (4), Gaussian correlation, plotted vs final state multiplicity. The $\pi^+\pi^+$ data are indicated by the box, $\pi^-\pi^-$ by the cross, and $\pi^+\pi^+,\pi^-\pi^-$ combined by the circle.

$\Delta Q^2/Q^2 \leq 7\%$ for the smallest bin in Q^2, which has the largest fractional difference.

In Fig. 21 the $\pi^+\pi^+$ and $\pi^-\pi^-$ distributions seem to be consistent with each other throughout the Q^2 range. We conclude from this that p-π^+ ambiguities do not play an important role in the shape of these distributions. There are overall normalization differences which we will discuss later in this paper. The $\pi^+\pi^+$, $\pi^-\pi^-$, and $\pi^+\pi^-$ distributions are also all similar at large Q^2. This suggests that the "source dynamics" seem to be independent of the sign of the pions.

At low Q^2 there are large differences between like- and unlike-sign ratios. The unlike-sign distributions display resonance structure at the invariant masses of the $\rho(770)$ and $f_2(1270)$. There are no $|Q|=2$ meson resonances. Thus no resonance structure (due to two-pion resonances) is seen in the like-sign ratios. However, the like-sign ratios show a significant increase compared to the unlike-sign ratios as Q^2 goes to zero. This can be taken as a possible indication of a low Q^2 probability enhancement for identical particles, as expected from Bose-Einstein correlations. The increase in the smallest Q^2 bin for the unlike-sign ratio is significant, but is due to electromagnetic final state interactions. This will be discussed in the next section.

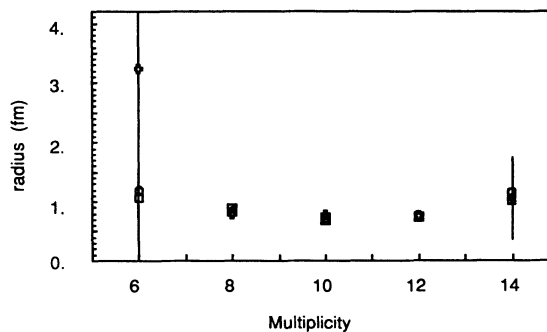We also note that the like-sign ratio low Q^2 enhance-

FIG. 27. Interaction volume radius from fits of function (5), Bowler correlation, plotted vs final state multiplicity. The $\pi^+\pi^+$ data are indicated by the box, $\pi^-\pi^-$ by the cross, and $\pi^+\pi^+,\pi^-\pi^-$ combined by the circle.

TABLE VII. Comparison of reaction volume radius with other experiments.

Reaction	$\sqrt{s}$ (GeV)	Radius (fm) Bowler	Gauss	Reference
$pp \rightarrow pp\ 2\pi^+2\pi^-$	7.21	3.11±10.9	1.16±0.63	E766
		1.07±0.35	0.97±0.15	
$pp \rightarrow pp\ 3\pi^+3\pi^-$	7.21	0.80±0.06	0.93±0.04	E766
		0.88±0.05	0.97±0.04	
$pp \rightarrow pp\ 4\pi^+4\pi^-$	7.21	0.80±0.03	0.98±0.03	E766
		0.70±0.03	0.88±0.02	
$pp \rightarrow pp\ 5\pi^+5\pi^-$	7.21	0.77±0.04	1.01±0.03	E766
		0.75±0.03	0.99±0.03	
$pp \rightarrow pp\ 6\pi^+6\pi^-$	7.21	1.05±0.68	1.41±0.41	E766
		1.02±0.30	1.29±0.19	
K^+p and π^+p	22		0.8±0.02	[19]
pp	31		~0.85	[22]
pp	26		1.02±0.2	[23]
pp	27.4		1.2±0.03	[24]
e^+e^-	29		0.65±0.04	[25]

ment does not vary dramatically for reactions (1a)–(1e). However, the high Q^2 behavior does vary both because of the change in the kinematic limits as a function of multiplicity and because of dynamics.

D. Other final state interactions

The correlations due to Bose-Einstein statistics for pions have the same effect as an attractive final state interaction. But pions can have other interactions with each other and with other particles in the final state due to both strong and electromagnetic forces. There is thought to be an attractive but weak $I = 2$ interaction between two like-sign pions [17]. The observed enhancements seen in Fig. 21 are larger than could be explained by this interaction. The electromagnetic final state interaction, also known as the "Gamow effect" [18], is repulsive for the like-sign case and attractive for the unlike-sign case. The increase in the unlike-sign ratio for the lowest Q^2 bin can be attributed to this attractive final state interaction [9]. The scale for such interactions is much smaller than the scales expected for other Q^2 structures. Such an effect is not expected to be observed in the like-sign case (where a "dip" would be expected), because for the repulsive case the integrated value of the effect for this Q^2 region is small. (In the attractive case the effect diverges.) Since both the scale and magnitude of the electromagnetic interaction are very small, we have not corrected the data for the effect.

In conclusion, the known two-body final state interactions do not provide a convincing explanation for the behavior of the Q^2 distribution ratios observed in Fig. 21.

E. Resonances

Resonances are ubiquitous in these data. Aside from the prominent $\rho(770)$ and $f_2(1270)$ seen in Fig. 21, there are π-nucleon resonances Δ^{++}, $N^*(1512)$, $N^*(1675)$, etc. Pions that are decay remnants of these resonances could affect the scale of the Bose-Einstein enhancement, since their source, a strong resonance, has a typical decay proper length of 1 fm. It is conceivable that the source distribution for resonant decay remnants would be different than for directly produced pions. Certainly, any model for source distributions would have to incorporate the effects of resonance production on such source distributions.

A more interesting idea is the possibility that the low Q^2 correlations observed in Fig. 21 are due *entirely* due to the presence of resonances. In fact, essentially pions have no data that are outside of resonance bands. Taking all two-particle invariant-mass combinations and excluding events with combinations within known resonance regions (mostly ρ and Δ^{++}) yielded 151 events out of 139 265 for reactions of the type (1a). Resonances would, in fact, cause a momentum correlation between like-sign pions.

The difficulties in understanding resonance effects stem primarily from having many possible small contributions and a lack of a good formalism with which to calculate the pion momentum distributions from a large number of wide resonances. We are continuing to study these effects, which will be the subject of a future paper.

TABLE VIII. Multiplicity dependence of interaction radius as a function of the number of pions (n_π) and number of pions per unit rapidity $(dn/d\eta)$.

Reaction	n_π	$\Delta\eta$	$dn/d\eta$	$R_G(++)$	$R_G(--)$
$pp\ 2\pi^+2\pi^-$	4	2.6	1.5	1.16±0.63	0.97±0.15
$pp\ 3\pi^+3\pi^-$	6	2.5	2.5	0.93±0.04	0.97±0.04
$pp\ 4\pi^+4\pi^-$	8	3.6	3.6	0.98±0.03	0.88±0.02
$pp\ 5\pi^+5\pi^-$	10	1.8	5.6	1.01±0.03	0.99±0.03
$pp\ 6\pi^+6\pi^-$	12	1.6	7.5	1.41±0.41	1.29±0.19

V. CORRELATION PARAMETRIZATION

A. Functional forms

We have used two functions to fit the ratio distributions of Fig. 18 for the like-sign pions. These two differ only in the correlation part of the $R(Q^2)$ function. The same source parametrization is used for both. These functions are the Gaussian correlation

$$R(Q^2)=(1+\alpha e^{\beta Q^2})\left[\lambda\left[1+\frac{\gamma}{(1+Q^2/\delta)^2}\right]\right] \qquad (4)$$

and the Bowler correlation

$$R_B=\left[1+\frac{\alpha}{(1+Q^2/\beta)^2}\right]\left[\lambda\left[1+\frac{\gamma}{(1+Q^2/\delta)^2}\right]\right]. \qquad (5)$$

The Bowler correlation was motivated by considerations given in Ref. [19]. The source function is the Fourier transform of an exponentially decreasing radial distribution of pion pairs. For both correlation functions, λ is the high Q^2 limit of the ratio. Both functions have five parameters. The parameters are determined by minimizing a χ^2 in a fit of the functions to the ratio histograms shown in Fig. 21. The central Q^2 value of each bin is used in the fit, with the expected error given by the statistical uncertainties in the numerators and denominators for each bin taken in quadrature. The correlation among the extracted parameters was found to be insignificant, but the errors quoted for the fitted values include correlations.

B. Results for different multiplicities

The results for the fits are shown in Tables III–VI and plotted in Figs. 22 ($\pi^+\pi^+$) and 23 ($\pi^-\pi^-$). The data are represented by crosses, with the horizontal bar indicating the bin width and the vertical bar the error. The χ^2 per degree of freedom for these fits is typically 1, indicating that functions (4) and (5) provide adequate descriptions of the ratios. Note that these fits are over the full range of Q^2 of Fig. 21. The lower curve in the figure corresponds to only the source part of $R(Q^2)$.

As a general observation, the source function parameters are consistent between the two sets of parametrizations. This supports the assumption that the source and correlation functions can be factored. That is, the difference observed in the correlation functions indicates that there is very little correlation in the fit between the parameters of the source and correlation functions.

The parameters for the Bowler and the Gaussian correlation functions have similar behavior. The term multiplying the Q^2-dependent part of the correlations, sometimes referred to as the "strength" term, is larger for $\pi^-\pi^-$ than for $\pi^+\pi^+$ ratios. This could be due to the dilution of the π^+ data by misidentified protons.

The parameters α and β from the fits are plotted in Figs. 24 (Gaussian) and 25 (Bowler). The parameter β can be interpreted as the source separation scale for each parametrization. Thus, for the Gaussian correlation function,

rms radius$=\hbar c\sqrt{3\beta}$,

and for the Bowler correlation function,

rms radius$=\hbar c\sqrt{6/\beta}$.

These are shown in Figs. 26 and 27. The $\pi^+\pi^+$ and $\pi^-\pi^-$ distributions are in excellent agreement with each other. There is no multiplicity dependence observed in the data.

VI. COMPARISONS WITH OTHER DATA

Table VII lists the results for the radius obtained in this experiment, together with those of previous measurements. In all cases, the errors quoted are statistical. When the initial particles are both protons, the radius seems to cluster around 1 fm. However, some of the errors are quite small and suggest that all the results are not consistent with each other.

Differences might be attributed to differences in the production mechanism. This is supported by the fact that changing the species of the initial particles affects the measured radius.

The multiplicity dependence of the radius has been studied in other experiments. High-energy pp and $p\bar{p}$ interactions and nuclei-nuclei collisions observe such multiplicity dependences. In terms of differential charged multiplicity observed in a pseudorapidity region ($\Delta\eta$) in Ref. [20], at $\sqrt{s}=630$ GeV, the radius was parametrized as

$$R_G=1.03+0.089\frac{\Delta n}{\Delta\eta} \text{ fm} .$$

This dependence agrees qualitatively with that found in other high-energy experiments [21] and with the results
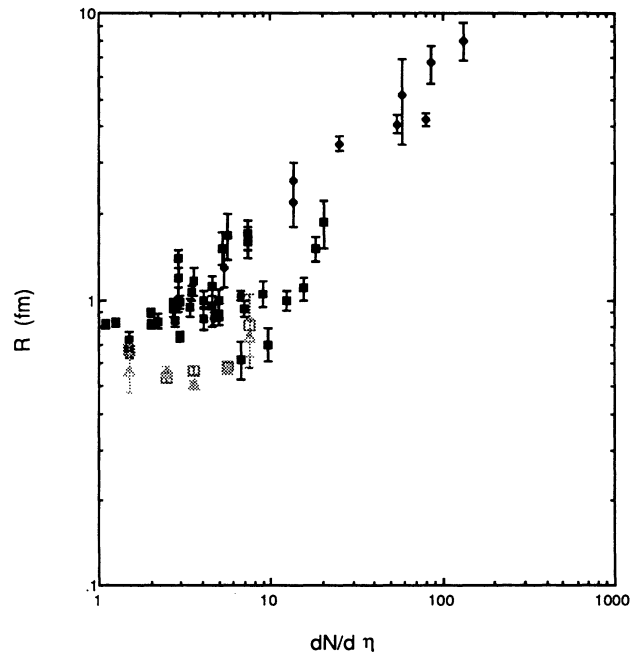

FIG. 28. Dependence of the interaction radius on $dn/d\eta$ for wide variety of beam and target particles and center-of-mass energies. The open symbols are data from this study.

of nuclei-nuclei collisions [10]. Our results from this kind of study are presented in Table VIII for each charge species and reaction type. Also tabulated are the pion multiplicities for each reaction and the full width at half maximum (FWHM) of the pion rapidity distributions. The ratio of pion multiplicity to the FWHM of the rapidity distribution is given as $\Delta n /\Delta\eta$. These radii are then extracted using three hypotheses: (1) the data do not depend on multiplicity, (2) the data depend linearly on n, the pion multiplicity, and (3) the data depend linearly on $\Delta n /\Delta\eta$. The first hypothesis yields

$$R_G(++)=0.982\pm0.019 \text{ fm}, \quad \chi^2/N_{DF}=3.7/4 ,$$

$$R_G(--)=0.987\pm0.024 \text{ fm}, \quad \chi^2/N_{DF}=2.7/3 ,$$

which agree with each other and provide good fits to the data. The second hypothesis results in the fits

$$R_G(++)=(0.773\pm0.019)+(0.020\pm0.012)n ,$$

$$\chi^2/N_{DF}=0.998/3 ,$$

$$R_G(--)=(0.899\pm0.112)+(0.008\pm0.014)n ,$$

$$\chi^2/N_{DF}=2.2/2 ,$$

which also give good fits. The slope parameters in both fits are consistent with zero. The third hypothesis resulted in

$$R_G(++)=(0.882\pm0.065)+(0.024\pm0.015)\frac{dn}{d\eta} ,$$

$$\chi^2/N_{DF}=1.2/3 ,$$

$$R_G(--)=(0.935\pm0.071)+(0.012\pm0.015)\frac{dn}{d\eta} ,$$

$$\chi^2/N_{DF}=2.1/2 .$$

Once again, the fits seem to be acceptable and the slope terms consistent with zero. We conclude that these data do not require a multiplicity dependence. The absence of a dependence of the radius on multiplicity at low center-of-mass energy agrees with the observation of Ref. [22]. Figure 28 shows these data in comparison with other experiments, as a function of the differential multiplicity $\Delta n /\Delta\eta$, assuming that rapidity and pseudorapidity are equivalent.

VII. CONCLUSIONS

This study of two-pion correlations isolated a large number of totally reconstructed events identified as reactions

$$p +p \rightarrow p +p +2\pi^+ +2\pi^- \tag{1a'}$$

$$\rightarrow p +p +3\pi^+ +3\pi^- \tag{1b'}$$

$$\rightarrow p +p +4\pi^+ +4\pi^- \tag{1c'}$$

$$\rightarrow p +p +5\pi^+ +5\pi^- \tag{1d'}$$

$$\rightarrow p +p +6\pi^+ +6\pi^- . \tag{1e'}$$

Two distinguishing characteristics of these data are the high-momentum resolution achieved by the spectrometer and the small backgrounds due to missing particles and particle misidentification. Using this well-defined sample of reactions and comparing the two-pion relative four-momentum (Q^2) distribution, we observed low Q^2 enhancements for both $\pi^+\pi^+$ and $\pi^-\pi^-$ consistent with each other and not inconsistent with measurements made by other experiments. Taking the hypothesis that these enhancements are the consequence of Bose-Einstein symmetry for the pions, the scale of the enhancement can be interpreted as the interaction volume radius, measured to be 0.98 fm both from $\pi^+\pi^+$ and $\pi^-\pi^-$ correlations. The interaction volume radius also appears to be independent of multiplicity for these data.

These results are consistent with previous observations, though the technique and data sample used by this study differ greatly from those used in other analyses of pion correlations.

[1] G. Goldhaber *et al.*, Phys. Rev. Lett. **3**, 181 (1959).

[2] G. Goldhaber *et al.*, Phys. Rev. **120**, 300 (1960).

[3] E. Fermi, Prog. Theor. Phys. **5**, 570 (1950).

[4] N. Xuong and G. R. Lynch, Phys. Rev. **128**, 1849 (1962); T. Ferbel *et al.*, *ibid.* **143**, 1096 (1966); V. Alles-Borelli *et al.*, Nuovo Cimento A **50**, 776 (1967); R. A. Donald *et al.*, Nucl. Phys. **B6**, 174 (1968); R. A. Donald *et al.*, *ibid.* **B11**, 551 (1969).

[5] G. E. Kopylov and M. K. Podgoretskii, Yad. Fiz. **15**, 392 (1972) [Sov. J. Nucl. Phys. **15**, 219 (1972)].

[6] For a comprehensive review of the experimental situation, see D. H. Boal, C-K Gelbke, and B. K. Jennings, Rev. Mod. Phys. **62**, 553 (1990).

[7] S. Pratt, Phys. Rev. D **33**, 1314 (1986); G. F. Bertsch, in *Quark Matter '88*, Proceedings of the Seventh International Conference on Ultrarelativistic Nucleus-Nucleus Collisions, Lenox, Massachusetts, 1988, edited by G. Baym, P. Braun-Munzinger, and S. Nagamiya [Nucl. Phys. **A498**, 173c (1989)].

[8] See, for instance, W. A. Zajc, in *Quark Matter '90*,

Proceedings of the Eighth International Conference on Ultrarelativistic Nucleus-Nucleus Collisions, Menton, France, 1990, edited by J. Blaizot *et al.* [Nucl. Phys. **A525**, 315c (1991)].

[9] L. R. Wiencke *et al.*, Phys. Rev. D **46**, 3708 (1992).

[10] Spectrometer performance article in preparation. Details can be found in the following theses: Michael Church, Ph.D. thesis, Columbia University, 1986; Benjamin Stern, Ph.D. thesis, Columbia University, 1988; Michael J. Forbush, Ph.D. thesis, Texas A&M University, 1990; Erik E. Gottschalk, Ph.D. thesis, Columbia University, 1992; Lawrence R. Wiencke, Ph.D. thesis, Columbia University, 1993; Jorge Uribe Duque, Ph.D. thesis, University of Massachusetts, Amherst, 1993.

[11] The z axis of the coordinate system is defined as the nominal direction. The y axis is the vertical, "up" being the direction of increasing y. The beam right direction defined x axis, explicitly this is $\hat{z} \times \hat{y}$. The coordinate system origin is set at the center of the magnetic field of the analyzing magnet.

[12] E. P. Hartouni *et al.*, Nucl. Instrum. Methods A **317**, 161 (1992); and (in preparation).

[13] J. A. Crittenden *et al.*, IEEE Trans. Nucl. Sci. NS-31, 1028 (1984). E. P. Hartouni, in "Workshop on High Sensitivity Beauty Physics at Fermilab," Fermilab Report No. UMAHEP-291, 1987 (unpublished).

[14] B. C. Knapp and W. Sippach, IEEE Trans. on Nucl. Sci. NS-27, 578 (1980); E. P. Hartouni *et al.*, *ibid.* NS-36, 1480 (1989); B. C. Knapp, Nucl. Instrum. Methods A **289**, 561 (1990).

[15] E. P. Hartouni and J. Uribe (unpublished).

[16] See, for instance, T. Åkesson *et al.*, Phys. Lett. B **155**, 128 (1985).

[17] M. G. Bowler, Z. Phys. C **39**, 81 (1988); H. Burkhardt and J. Lowe, Phys. Rev. Lett. **67**, 2622 (1991).

[18] G. Gamow, Z. Phys. **51**, 204 (1928).

[19] M. Adamus *et al.*, Z. Phys. C **37**, 347 (1988).

[20] C. Albajar *et al.*, Phys. Lett. B **226**, 410 (1989).

[21] See, for example, T. Alexopoulos *et al.*, Phys. Rev. D **48**, 1931 (1993).

[22] A. Breakstone *et al.*, Z. Phys. C **33**, 333 (1987).

[23] J. L. Bailly *et al.*, Z. Phys. C **43**, 341 (1989).

[24] M. Aguilar-Benitez *et al.*, Z. Phys. C **54**, 21 (1992).
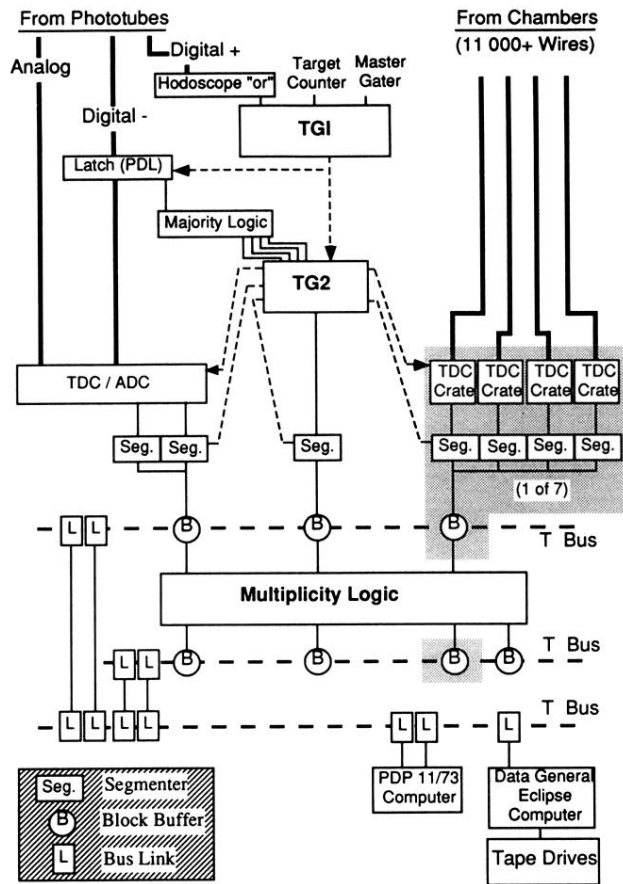
[25] H. Aihara *et al.*, Phys. Rev. D **31**, 996 (1985).

FIG. 2. Block diagram of BNL E766 data acquisition system.